

Chapter 3

Numerical Simulation Model

F. Stroscher, A. Schirrer, M. Valášek, Z. Šika, T. Vampola, B. Paluch,
D. Joly, C. Breitsamter, M. Meyer, D. Paulus, T. Klimmek and H. Baier

3.1 Introduction

F. Stroscher and A. Schirrer

The active control design activities in ACFA 2020 are based on a numerical flight simulation model of the BWB aircraft configuration which shall predict its flight dynamics, as well as structural dynamic response. The classical approach of aircraft flight simulation is a 6 degrees of freedom flight dynamic model, not considering the dynamic response (that is, vibrations) of the airframe, as well as its impact on the flow field around the wetted surface. Aircraft structural dynamics are classically considered in structural loads analysis (for example, landing loads) and aeroelastic stability (for example, flutter) or response analysis (for example, transient gust response). This separated approach is well suited for flight simulation of classical wing-fuselage aircraft whose aeroelastic response does not remarkably interact with its flight dynamics.

However, for larger aircraft with high wing spans, aerodynamic coupling between flight dynamic and aeroelastic motion becomes more significant because wing vibration frequencies are lower and closer to those of the flight dynamic modes

F. Stroscher (✉) · C. Breitsamter · M. Meyer · D. Paulus · H. Baier
Technische Universität München, Munich, Germany
e-mail: stroscher@lb.mw.tum.de

A. Schirrer
Vienna University of Technology, Vienna, Austria

M. Valášek · Z. Šika · T. Vampola
Czech Technical University in Prague, Prague, Czech Republic

B. Paluch · D. Joly
ONERA, Châtillon, France

T. Klimmek
German Aerospace Center, Cologne, Germany

(for example, the short-period mode). This holds true for the ACFA 2020 BWB aircraft, which is even more prone to such interactions due to the following properties: First, its airframe is highly flexible compared to wing-fuselage aircraft. The low wing loading, achieved by the fuselage acting as lifting surface, allows for a lightweight, thin and thus flexible wing design. Second, a significant aerodynamic coupling of flight dynamic and aeroelastic motion is present because the wide wing-like fuselage is involved in structural deformations. This behavior is well observable at the first bending mode, which clearly shows wing deflection, but also pitch rotation of the fuselage. Consequently, the aerodynamic coupling of aeroelastic and flight dynamic degrees of freedom will be considered in the BWB aircraft flight simulation model.

For control design, a linearized simulation model in the time domain is required. It shall be parametric with respect to multiple mass configurations of the aircraft, as well as flight conditions. Its numerical order has to be relatively low in order to efficiently perform parametric control studies. The state-space formulation is applied for the formulation of the aircraft equations of motion. The state vector \mathbf{x} is comprised of the plant degrees of freedom and their first time derivatives. The input Eq. (3.1) is a first-order differential equation, relating the state vector time derivative to the state vector by the system matrix \mathbf{A} and the input vector \mathbf{u} by the input matrix \mathbf{B} . The output Eq. (3.2) relates plant outputs to the state variables and inputs by the output matrix \mathbf{C} and the feed-through matrix \mathbf{D} .

$$\dot{\mathbf{x}} = \mathbf{A}\mathbf{x} + \mathbf{B}\mathbf{u} \quad (3.1)$$

$$\mathbf{y} = \mathbf{C}\mathbf{x} + \mathbf{D}\mathbf{u} \quad (3.2)$$

This chapter outlines two approaches to obtaining a numerical simulation model suitable for dynamic simulation studies and for control design (after performing further order-reduction, see Chap. 4):

- In the initial phase of the ACFA 2020 project, a predesign model of a large 750-passenger BWB aircraft configuration has been made available by the NACRE project consortium [2] to the ACFA 2020 consortium. This way, the development of the necessary methods and tools for modeling, order-reduction, and control design could be started early in the project during the conceptual design phase leading to the ACFA 2020 flying wing design. Section 3.2 reports on the necessary adaptation tasks to the NACRE BWB configuration to enable control-related dynamic simulation, see also [8].
- The actual modeling tasks of the selected ACFA BWB configuration are presented in Sects. 3.3–3.5. Section 3.3 reports on the structural modeling via the finite element method (FEM). An FE model of the airframe is utilized for the computation of its natural modes, which are used as a reduced set of degrees of freedom for the aeroelastic equations of motion. Section 3.4 outlines aerodynamic modeling and analysis tasks. High-fidelity as well as standard aerodynamic tools are applied for the computation of the aerodynamic database. On the one hand, steady aerodynamic derivatives of the rigid aircraft are required for flight dynamic modeling. On the other hand, unsteady aerodynamic forces on modal coordinates,

so-called generalized aerodynamic forces (GAF) will be derived. The reduction of structural and aerodynamic degrees of freedom to a limited number of common modal coordinates is a highly effective model order reduction principle, which is common practice in aeroelastic simulation. Finally, the coupled flight dynamic and aeroelastic equations of motion will be derived from structural dynamic and aerodynamic data in Sect. 3.5. The nonlinear flight dynamic equations of motion are coupled to the aeroelastic equations of motion. The linear state-space model is derived by numerical linearization of the coupled equations.

3.2 Preliminary Structural Modeling

M. Valášek, Z. Šika and T. Vampola

This section describes the adaptations on the finite element (FE) model of the flying wing configuration of the starting structure, a BWB aircraft configuration laid out for 750 passengers that has been made available by the NACRE project [2]. This model was utilized in the initial phase of the ACFA 2020 project for developing, testing, and tuning the modeling and control design methods that were later applied to the ACFA 2020 BWB configuration (designed for 450 passengers).

An overview on the performed model modifications is given in [8]. The structural modifications detailed in the following were necessary to achieve a structural model applicable for structural dynamic analysis for different mass configurations. Starting point of the adaptation was the FE model of the primary structure of the flying wing configuration. The model was examined regarding structural dynamic and structural stability (buckling) characteristics. To eliminate the detected and unwanted local modes, additional structural elements in the form of beams were integrated. Furthermore, some missing parts in primary structure like tail, engines, pylons, and cockpit were modeled. In addition, masses were incorporated for the consideration of the fuel and other nonstructural components. Finally, a structural dynamic analysis was performed for various mass configurations.

3.2.1 Testing FEM Structure

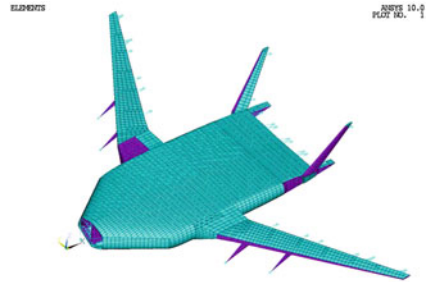
All designed methods and concepts used for the optimal design of the flying wing were tested and tuned on the simplified flexible structure. Due to the size of the flexible model was used for only so-called primary structure and the missing parts (tail, fuel masses, engines, nonstructural masses) have been modeled as a discrete mass in the primary structure (Figs. 3.1 and 3.2).

The FE model of the primary structure was scrutinized in order to detect causes for the poor structural dynamic characteristics. The model was examined regarding structural dynamic and structural stability (buckling) characteristics. To eliminate

Fig. 3.1 Primary structure
(made available by the
NACRE project [2])



Fig. 3.2 Modified testing
structure of the flying wing



the detected and unwanted local modes, additional structural elements in the form of beams were integrated to the primary structure to reinforce the fuselage of the testing structure of the flying wing. The geometric configurations of the added beams were derived from the buckling analysis. The calculated allowable stresses gave hints for the designer to adapt the thickness of various shell elements of the structure. The reinforcement of the fuselage on the contrary increases the total mass of the flying wing. The additional beams were used in the fuselage and transition areas (Fig. 3.3).

The original primary structure contained not all structural parts of the aircraft. The biggest missing part was the tail. Therefore, the tail structure was connected to the primary structure. In order to reduce the size of the model, only the load carrying parts were used. The leading and trailing edges for the vertical tails were left out. The structure of the rudder was replaced by a simple plate structure. This allowed for the consideration of control surface modes (Fig. 3.4).

As for the fuselage, beam elements were integrated to stiffen the structure in order to avoid parasitic modes. In contrary to the stiffening structure for the fuselage, the additional beam elements have no mass. This was done to simplify the process to balance the center of gravity (CG) position of the overall structure including nonstructural components. Otherwise, a more extensive dimensioning process would have been necessary.

The engines were modeled as one mass point at the CG of the engine. For the pylons, a simple beam structure was applied to achieve a distributed connection of the pylon to the wing box. By varying the structural properties of the beams, realistic structural dynamic characteristics of the engine/pylon structure were achieved (Fig. 3.5).

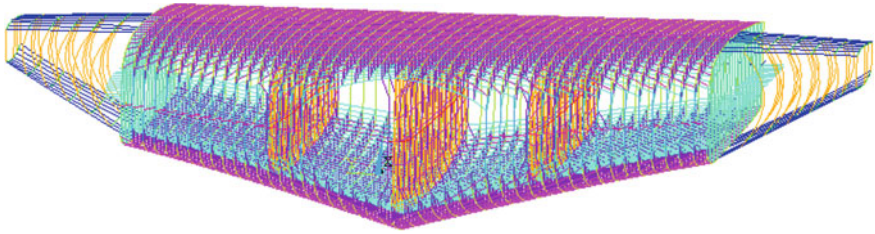


Fig. 3.3 Additional stiffening elements in the fuselage and transition areas of the testing structure

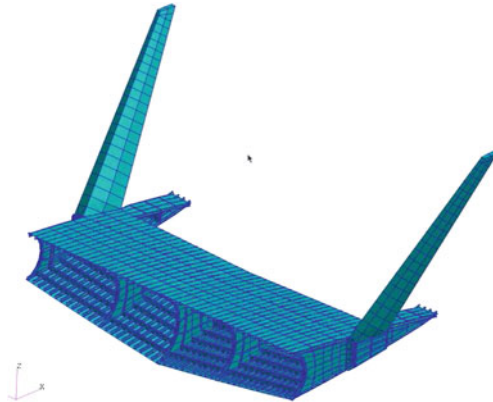


Fig. 3.4 FE model of tail structure

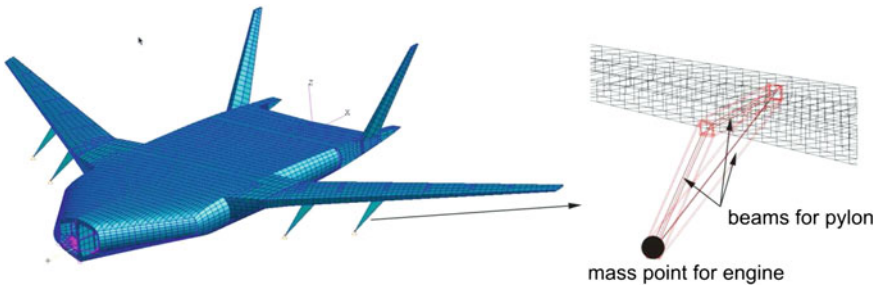
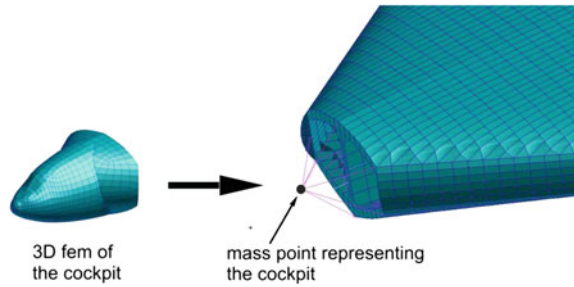


Fig. 3.5 Model of engines and pylons

A single mass point was used for representing the cockpit. The mass and the location were taken from the mass value and the CG position of the detailed structural model of the previous project modeling complete aircraft model (Fig. 3.6).

The fuel tank masses were modeled as concentrated masses distributed in the wing. For the tanks 1 and 2, the fuel is represented by only one mass point. For tanks 3 and 4, mass points per sections between two ribs are designated. The breakdown of the masses for tanks 3 and 4 for full fuel tanks is proportional to the volumes

Fig. 3.6 Cockpit structure

of each section. For the state-space models, different fuel configurations have to be taken into account. Therefore, a widespread applied strategy was used by emptying the tanks from inside of the wing to outside. This approach brings out a relief of the root bending moment of the wing due to fuel masses (Figs. 3.7, 3.8 and 3.9).

The additional nonstructural masses were redistributed in the fuselage modeling the loads. The mass points were connected to the structure by using a connection element (RBE3 element) that defines a constraint relation in which the motion at a “reference” grid point is the least square weighted average of the motions at other grid points. The element is useful for “beaming” loads and masses from a “reference” grid point to a set of grid points. The overview of the distribution of the nonstructural masses in the plane is introduced in Fig. 3.10.

For testing purpose of assembled flexible structural model were suggested the loading cases for that were computed the mean aerodynamic chord (MAC) to prove the quality of the model and compare the assembled structure with previous concepts of the flying wing. The loading cases were realized according to Fig. 3.11.

For the different load cases were computed positions of the CGs. The CG position is crucial for the stability of the structure. It was tuned according to similar structures to obtain reasonable values (Fig. 3.12).

Due to the needs of the driving algorithms, the validity of the structural model was tested by the conditions of the symmetry too (Fig. 3.13).

The eigenfrequencies for the right half and left half of the model were compared for chosen mass configuration. The boundary condition was applied in the plane of symmetry. The differences between eigenfrequencies of the left and right half of the structural model were computed. For the first 30 structural eigenmodes was the maximal frequency difference between left and right half of the model for all mass variants is below 0.3 Hz. It means that the symmetry of the structural model was very good and assembled model could be used for testing of the derived methods and concepts for the optimal design of the ACFA flying wing. The total frequency densities of the assembled flexible structure were in a good accordance with the previous concepts of the flying wings structure without parasitic modes in the frequency range 0–30 Hz (Figs. 3.14, 3.15 and 3.16).

In the next step, the shear and normal forces and bending torques in the wings root were computed.

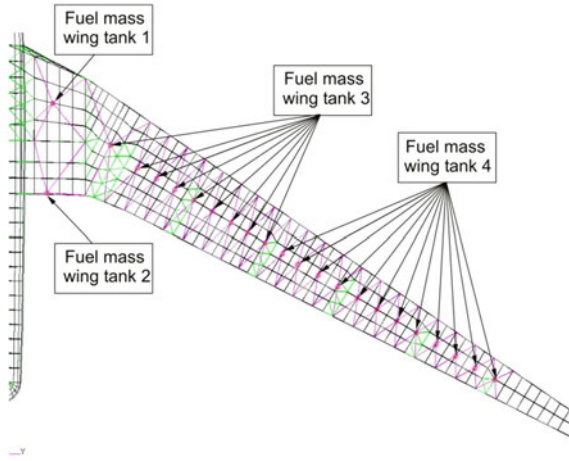


Fig. 3.7 Fuel masses in the wing tanks

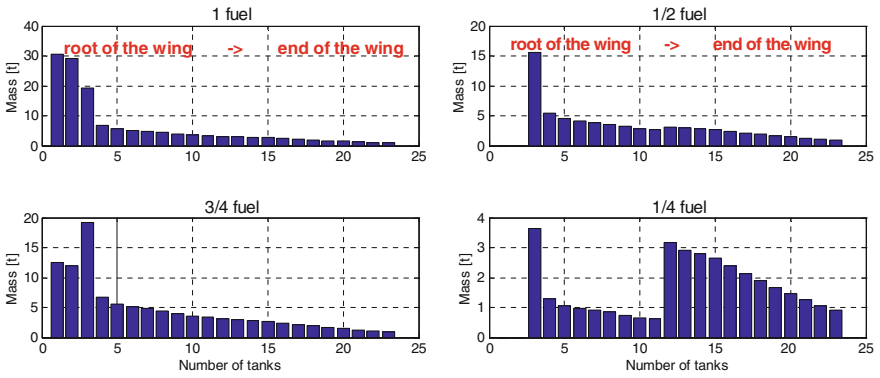


Fig. 3.8 Emptying strategy of the fuel tanks

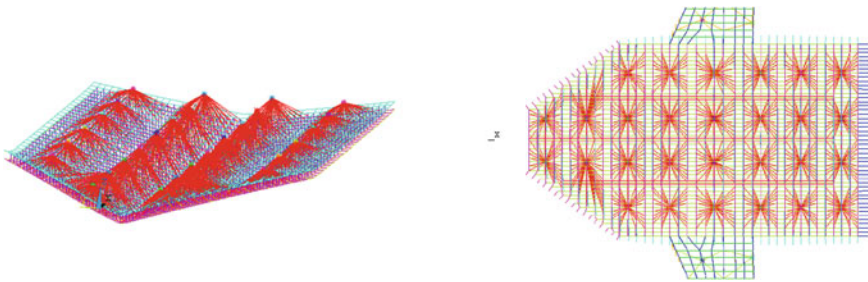


Fig. 3.9 Lumped masses in the testing structure of the flying wing

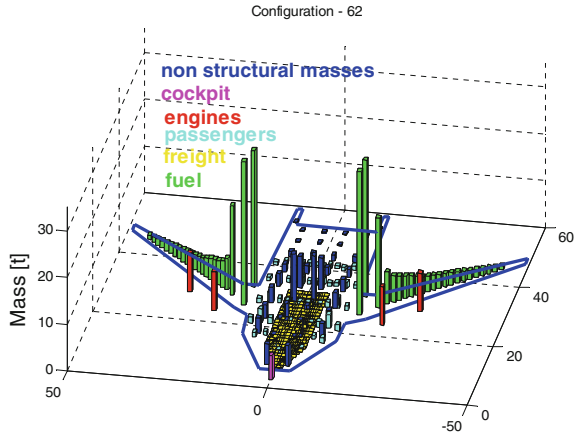


Fig. 3.10 Distribution of the nonstructural masses in the plane

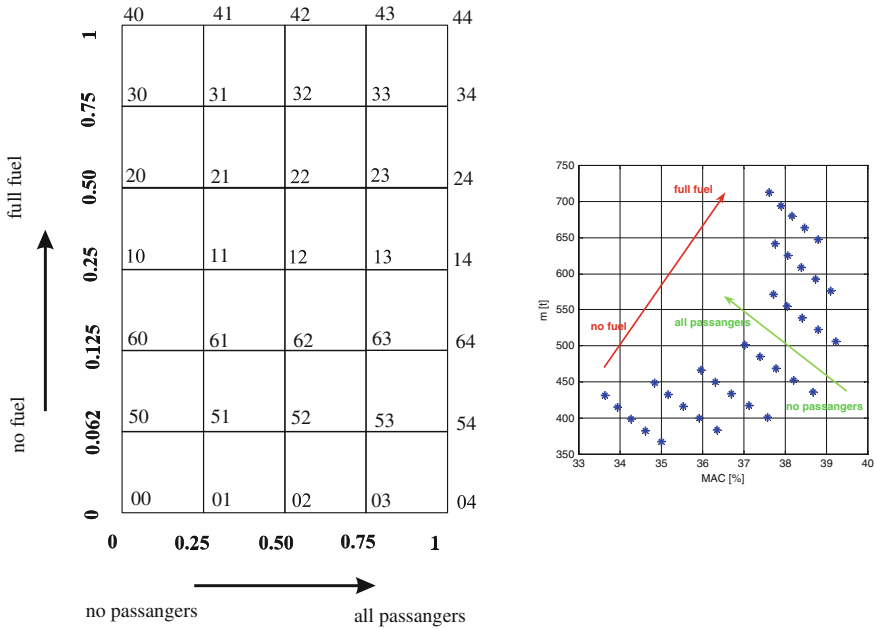


Fig. 3.11 Definition of load cases

Finally for the proved flexible structure of the flying wing, the result mass and stiffness matrixes for the all load case configurations were generated and a first hundred eigenmodes were computed. These information were used for deriving the reduced-order model (ROM) (Fig. 3.17).

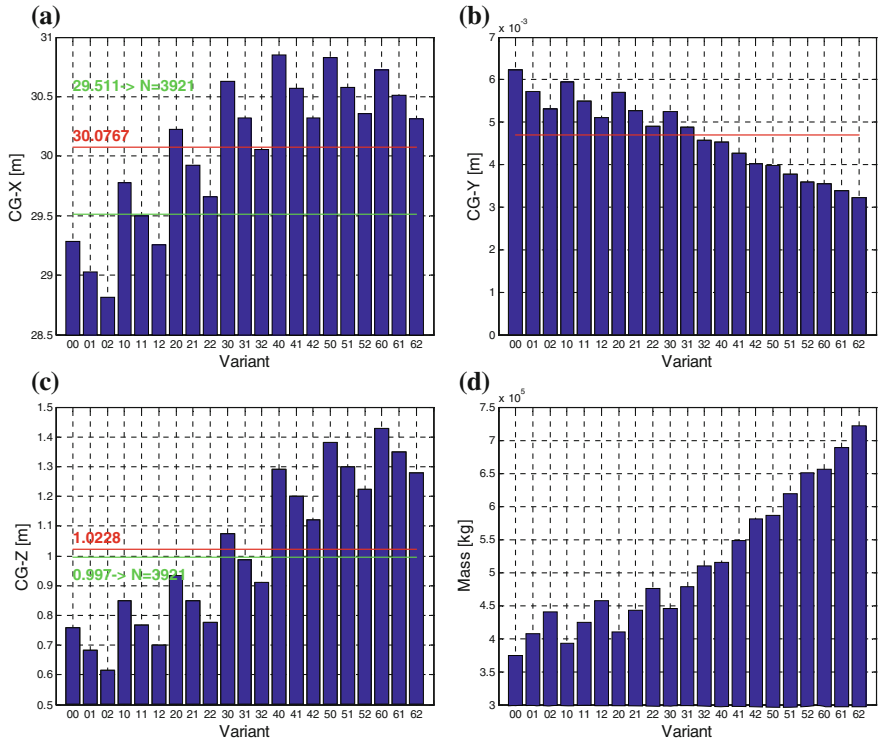


Fig. 3.12 Center of gravity positions of load cases. **a** CG x. **b** CG y. **c** CG z. **d** Mass variants

3.3 ACFA BWB Structural Modeling

B. Paluch and D. Joly

3.3.1 Overview on Structural Modeling

This section describes the step adopted for the construction of the BWB FE model within the framework of the ACFA program. After a brief description of the aircraft geometry and the configuration as well as the material properties, more realistic loading cases were determined in agreement with AIRBUS. The single shell concept used for the fuselage was validated through a detailed calculation which led to reinforce the initial structure to improve its buckling behavior. After having taken into account the distributions of the nonstructural masses, finite element calculations showed that the maximum strain criterion is satisfied. The aircraft mass breakdown and inertia parameters could then be determined from this model (Figs. 3.13, 3.14 and 3.15).

Fig. 3.13 Structural model—left half

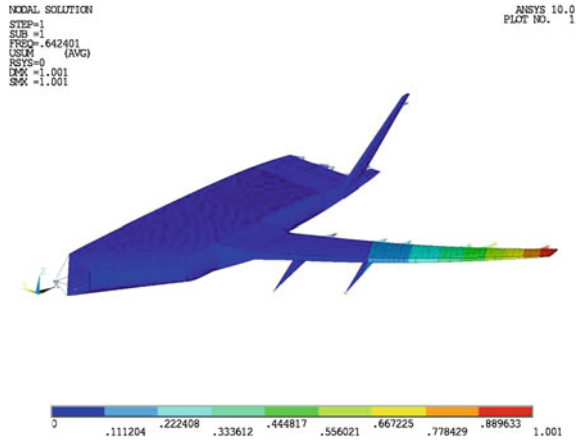
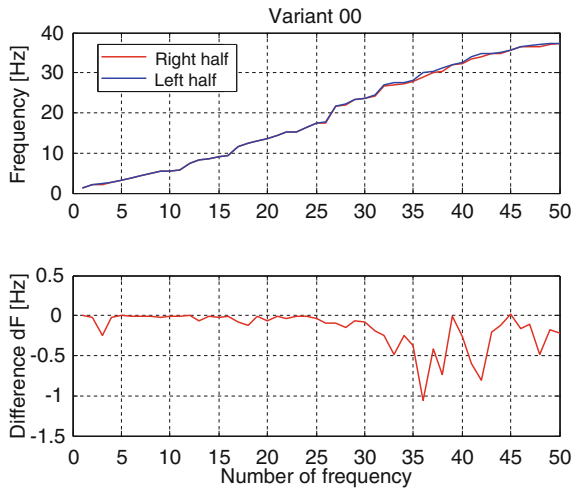


Fig. 3.14 Variant 00—frequency differences

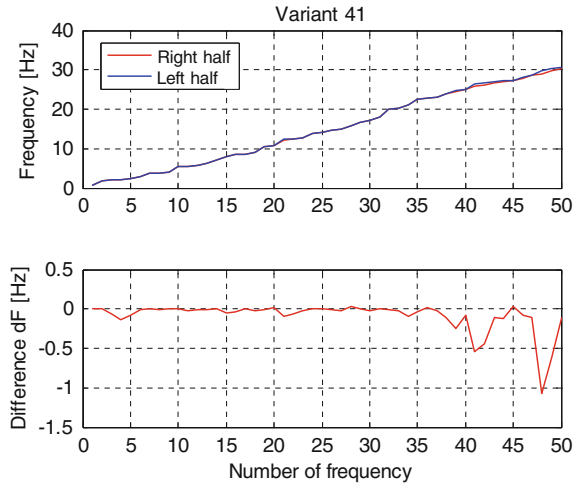


Because of the shape and the structural complexity of the BWB, the usual assumptions related to strength could become too restrictive. Consequently, an FE has been built to calculate the thickness of the various components. The evaluation of a new configuration is generally carried out on three levels:

Conceptual: starting from the aircraft mission specifications global results concerning the most adapted aircraft geometry and performances are obtained. Simple calculation procedures and expert knowledge are employed and the internal structure of the aircraft is not considered.

Preliminary: starting from more detailed specifications, a more precise weight estimation of the primary and secondary structures is done, requiring more refined computer codes, such as the FEM.

Fig. 3.15 Variant 41—frequency differences



Detailed: details (for example, technological constraints due to manufacturing) of most of the aircraft parts or components are considered, leading to a precise evaluation of the performances and costs of the project.

In this project, the design dedicated to the aeroelastic evaluation of this BWB concept is more relevant on a preliminary level than on a conceptual one. The main problem in the design step is to know the size of the smallest structural component that one should take into account in the FE model. For the BWB, this size has been limited to the frames and the stiffeners. Smaller components such as stringers, which play an important role for elastic stability of fuselage and wing skins, for example, were not meshed but included in the skin properties. In this manner, an FE model could be built with a reasonable but sufficiently large number of nodes and elements, allowing to perform an accurate analysis concerning flutter, weight estimation, and design evaluation.

3.3.2 ACFA Geometry

3.3.2.1 Overall Configuration

The geometry of the BWB configuration was defined in the reference document published in July 2008 by Technical University of Munich (TUM). The plane form of the aircraft is shown in Fig. 3.18: the overall length and span are equal to about 43 and 80 m, respectively.

In this document, the following zones are distinguished in the structural concept and in the FE model, respectively (Fig. 3.19):

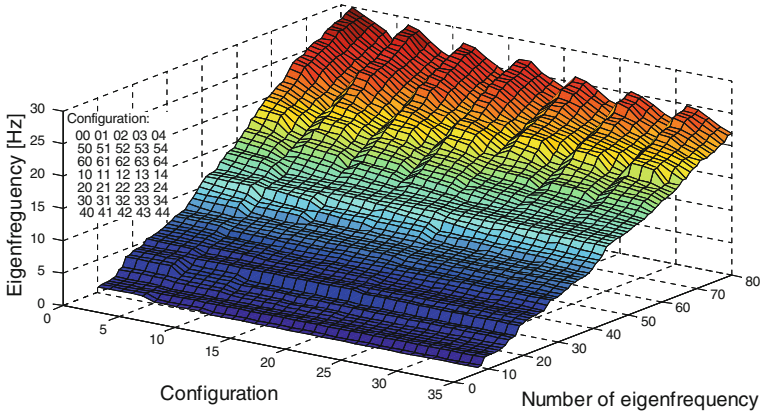
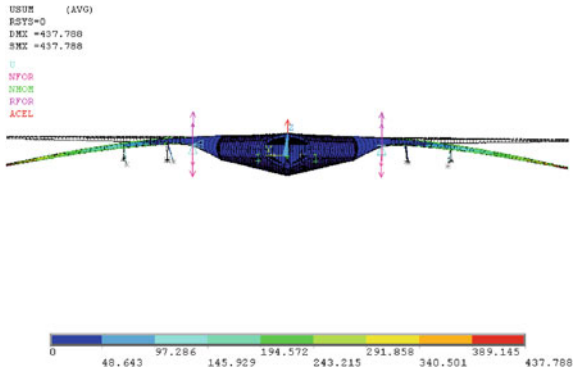


Fig. 3.16 Eigenfrequencies over load cases

Fig. 3.17 Testing structure—static deformation 2g



- the passengers cabin (pressurized),
- the cockpit (pressurized),
- the rear fuselage,
- the transition area (located between the cabin and the wing),
- the wing box,
- and the winglet box located at the wing tip.

Schematically, an aircraft structure can be split into two parts:

- the *primary* structure, designed to support the main loads such as aerodynamics, cabin pressurization, and so on. The different zones defined previously are included in this category,
- and the *secondary* structures which do not support the main loads, grouped in the following devices:
 - the aerodynamic devices like flaps (colored in blue in Fig. 3.19) and slats (green in Fig. 3.19),

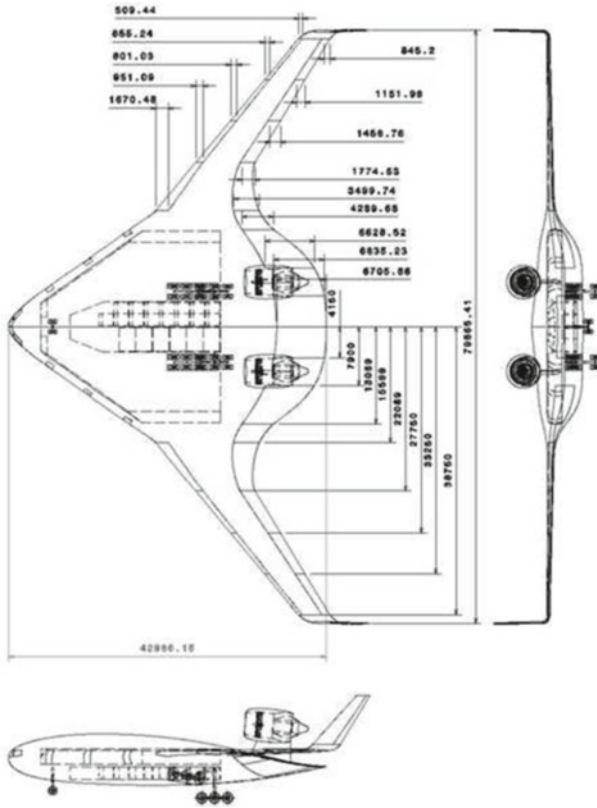


Fig. 3.18 ACFA BWB overall dimensions

- the tanks,
- the engines,
- the “active” components (actuators, ...),
- the “passive” components (seats, ...).

All the devices attached to the primary structure do not affect the resistance of the primary structure.

3.3.2.2 External Geometry

The external geometry of the aircraft was defined by a set of airfoils whose coordinates were communicated to ONERA by TUM. The global aircraft geometry reference frame (Fig. 3.20) is defined by:

- the frame origin O located at the aircraft nose,
- the X axis directed backward (from the cockpit to the rear),

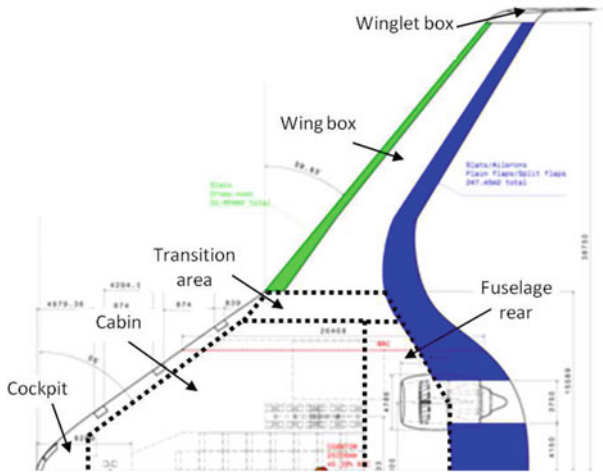
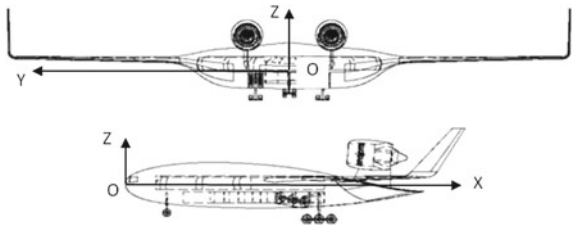


Fig. 3.19 BWB main structural parts

Fig. 3.20 BWB reference frame



- the Y axis directed from the fuselage center to the wing tip,
- and the Z axis defining a direct reference frame with the previous axis (and directed upward).

Except for the winglets (whose airfoil are defined in planes parallel to the XOY plane), the aircraft was defined by a series of airfoils whose coordinates are expressed in planes parallel to the XOZ plane, and for several positions in span (along the Y axis). The external shape can be defined by ruled surfaces between two consecutive airfoils.

3.3.2.3 Internal Geometry

Cabin volume was designed to obtain a capacity of 470 passengers divided into two classes (business class (BC) and economy class (YC)) on one deck. The cargo bay is designed to have a capacity of 30 LD3s (that is, 12 pallets). The rear landing gear boxes are located on both sides of the cargo bay as indicated in Fig. 3.21. The

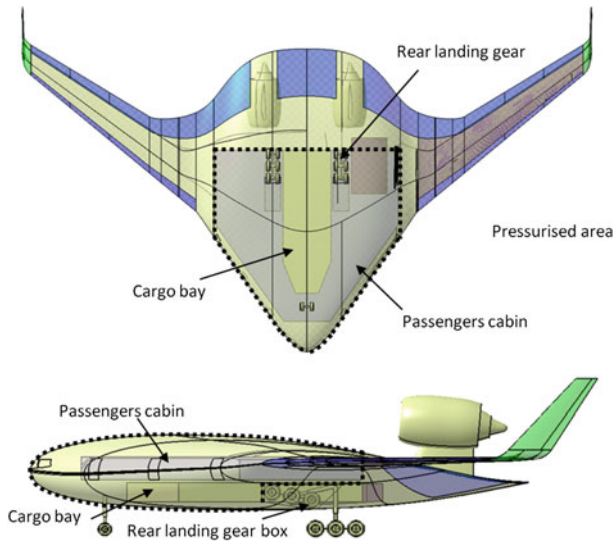


Fig. 3.21 CAD view of cabin and cargo bay locations in the BWB fuselage

pressurized volume of the cabin is thus defined (Fig. 3.21) by the external surface of the fuselage, the cabin bulkheads, and the lateral walls between the cabin and the transition area. Since the landing gear bays are not included in this pressurized volume, they will not be modeled as structural elements.

The pressurized area will be the subject of a specific structural concept developed in preceding European programs (VELA and NACRE). The rear part of the fuselage (non-pressurized) is delimited by the rear cabin bulkhead and the wall which will have to support the flaps. In the same way, the wing box is delimited by the leading and trailing edge spars which respectively support the four slats and the flaps (Fig. 3.22).

3.3.3 Material Properties

3.3.3.1 Composite Materials

The major part of the structure will be manufactured with carbon fiber/epoxy matrix laminates. C. Dienel from DLR-FA listed the advantages and the disadvantages (Table 3.1) of the various processes which could be used to manufacture the structure: hand lay-up, prepregs, or liquid composite molding (LCM).

According to Table 3.1, DLR deduced that it would be preferable, in terms of mechanical properties to production cost ratio, to use composites worked out by LCM. If the mass of the aircraft obtained with LCM composites would be too high, DLR-FA then recommends to choose prepregs, in order to save mass.

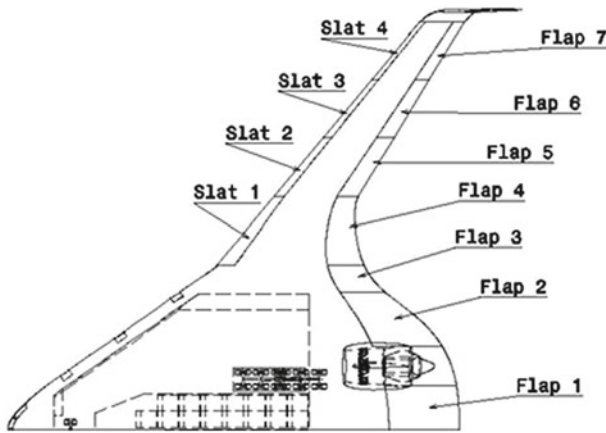


Fig. 3.22 Positions of flaps and slats

Another important material property is volumetric mass. TUM decided to take a volumetric mass of $1,800 \text{ kg/m}^3$ for all composite materials due to the local reinforcements. Since this work concerns a preliminary design, the mass will be evaluated without considering the structure details. Some parts of the structure will be made up of a combination of structural elements, such as the wing and cabin skins. In both cases, the composite panels are stiffened by stringers.

To size the structure, a yielding stress criterion is required, and AIRBUS Hamburg suggested to use the following allowable strains for all considered composite materials:

Ultimate loads:

$$|\varepsilon| \leq \varepsilon_{\text{ult}} = 0.5\% \quad (3.3)$$

Table 3.1 Qualitative evaluation of current composite manufacturing processes (from C. Dienel, DLR-FA)

	Hand lay-up	Prepreg technology	Liquid composite molding (LCM)
Initial cost	Low	High	Medium
Tooling costs	Low	High	High
Labor costs	High	Medium	Medium
Material costs	Low	High	Low
Series volume	<1,000 p.a.	<3,000 p.a.	<50,000 p.a.
Cycle time	3–24 h	5–24 h	15 min–24 h
Mechanical properties	Modest	Very good	Good
Quality	Modest	Very good	Good

Limit loads:

$$|\varepsilon| \leq \varepsilon_{\text{lim}} = \frac{1}{1.5} \varepsilon_{\text{ult}} = 0.35 \% \quad (3.4)$$

This value has been obtained by dividing the ultimate load by a factor of 1.5. The allowable value for limit loads takes into account the margins due to fatigue and damage tolerance. The criterion which will be used contains the maximum absolute value of the principal strain, such as:

$$\varepsilon = \max(\varepsilon_{\text{I}}, \varepsilon_{\text{II}}) \quad (3.5)$$

This value is compared with one of the two values (3.3) and (3.4), depending on the studied load case, assuming that the allowable strains are identical in tension and compression.

3.3.3.2 Other Materials

Other materials which could be used in the structure design are essentially aluminum alloys with the following characteristics (recommended by TUM for a current alloy):

- Young's modulus $E = 70 \text{ GPa}$
- Poisson's coefficient $\nu = 0.3$
- yield strength $\sigma_e = 300 \text{ MPa}$ which leads to a yield strain of about 0.4 %
- volumetric mass $\rho = 2,750 \text{ kg/m}^3$.

3.3.3.3 Technological Constraints

A major technological constraint is the minimal thickness of a laminate. For the skins, this thickness could be relatively small. However, composite materials being not ductile, possible impacts can cause more serious damage to composites than to metals. For the skins, AIRBUS recommends to use a minimal thickness of 2 mm in order to preserve a sufficient level of laminate damage tolerance.

3.3.4 Load Cases

3.3.4.1 Cabin Pressurization

The maximum pressure difference in the passenger cabin and the cockpit, at the highest flight altitude, is $\Delta p = 0.7 \text{ bar}$. This value corresponds to the difference between the cabin and the atmospheric pressure, multiplied by a safety factor. Two cases have to be considered:

- limit pressure with $\Delta p = 0.7$ bar
- ultimate pressure with $\Delta p = 0.7 \text{ bar} \times 2 = 1.4$ bar

The second case corresponds to the cabin pressure test. During the sizing step, this case will be considered apart from the other load cases.

3.3.4.2 Aerodynamic Loads

The total lifting force L acting on the half-BWB is given by the relationship:

$$L = \int_0^{Y_T} l(y) dy = \frac{1}{2} M g f_L \quad (3.6)$$

where M is the mass of the aircraft (MTOW, MZFW, ...) depending on the considered flight configuration, g the acceleration of gravity (9.81 m/s^2), and f_L the load factor. Let be:

$$\Delta Y_t = \frac{1}{3} (Y_E - Y_F) \quad \text{and} \quad \Delta Y_w = \frac{2}{3} (Y_E - Y_F) \quad (3.7)$$

the lengths of the second zone, where the subscripts t and w are related to the second and last third of the wing span, respectively. The lifting force is then equal to:

$$L = \left(\frac{1}{2} \Delta Y + \Delta Y_w + Y_F \right) l_{\max} \quad (3.8)$$

from where one can easily deduce l_{\max} and consequently the aerodynamic pressures exerted on the fuselage (p_f) and the wing (p_w), given by:

$$p_w = \frac{l_{\max} \Delta Y_w}{A_w} \quad \text{and} \quad p_f = \frac{l_{\max} Y_F}{A_f} \quad (3.9)$$

where A_f and A_w are the projected areas of the fuselage and the $2/3$ wing, respectively. For the fuselage, as for the wing, one considers the total projected area (from the leading edge toward the trailing edge), that is, the area including slats and flaps.

The calculation of the pressure distribution to be taken into account in the FE model will be based on an elliptic distribution. The two values of mass (for the half-BWB) to consider for the calculation of this new pressure distributions are $MTOW = 200 \text{ t}$ and $MZFW = 151 \text{ t}$. The calculation has been performed considering the following law for the kinetic lifting force l :

$$l = l_{\max} \sqrt{1 - \left(\frac{Y}{Y_E} \right)^2} \quad (3.10)$$

Together with (3.9), the following relationship results:

$$L = \sum_{i=1}^N l_i(Y) \Delta Y_i = l_{\max} \sum_{i=1}^N \sqrt{1 - \left(\frac{Y_i}{Y_E}\right)^2} \Delta Y_i = \frac{1}{2} M g f_L \quad (3.11)$$

Equation (3.11) allows to calculate l_{\max} by carrying out the summation on a number N of slices along the span Y . For the three loading cases considered hereafter, the following values have been calculated:

- Case A: $l_{\max} = 161,228 \text{ N/m}$ for $M = 200 \text{ t}$ (MTOW of the half-BWB) with $k = 2.5$
- Case B: $l_{\max} = 121,727 \text{ N/m}$ for $M = 151 \text{ t}$ (MTOW of the half-BWB) with $k = 2.5$
- Case C: $l_{\max} = 64,491 \text{ N/m}$ for $M = 200 \text{ t}$ (MTOW of the half-BWB) with $k = 1$

To calculate the pressure field, it is necessary to take into account the chord variation law according to Y . The chord is interpolated linearly between two reference airfoils. For each section located at a Y_i position, the pressure p_i is given by:

$$p_i = \frac{l_{\max}}{c_i} \sqrt{1 - \left(\frac{Y_i}{Y_E}\right)^2}, \quad (3.12)$$

where c_i is the local chord at position Y_i . The pressure distribution calculated according to (3.12) gives, a priori, a load case more unfavorable than that initially proposed by TUM. In Fig. 3.23 the strong differences due to the various Cases A–C are shown.

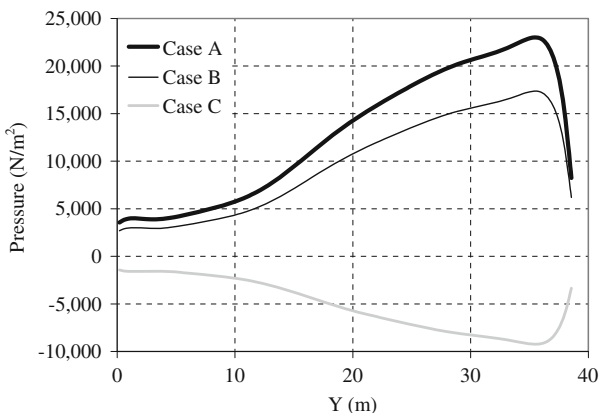


Fig. 3.23 Pressure distributions calculated for the load Cases A, B, and C

Table 3.2 Load cases considered for the BWB sizing

Load			Maximum strain (%)	Mass		Load factor		Cabin pressure (bar)
Case	Subcase	Type		Type	Value (t)	Aero. (g)	Inertia (g)	
A	1	Limit	0.34	MTOW	200.0	2.5	-2.5	-
	2	Limit	0.34	MTOW	200.0	2.5	-2.5	0.7
B	1	Limit	0.34	MTOW	151.0	2.5	-2.5	-
	2	Limit	0.34	MTOW	151.0	2.5	-2.5	0.7
C	1	Limit	0.34	MTOW	200.0	-1.0	1.0	-
	2	Limit	0.34	MTOW	200.0	-1.0	1.0	0.7
D	1	Ultimate	0.50	-	-	-	-	1.4

3.3.4.3 Load Cases Summary

The various loading cases, which have to be considered to size the primary structure, are summarized in Table 3.2. The positive sign means that the loads are applied upward (that is, on the lower side for the aerodynamic loads), while the negative sign means that the loads are directed downward. For the first three Cases A, B, and C, the inertia loads are always applied in the opposite direction to the aerodynamic loads. In the Case D, one considers only the ultimate cabin pressure without any other load.

3.3.5 Structural Concepts

3.3.5.1 Passengers Cabin

The structural concept adopted by ONERA for the pressurized part of the fuselage is that which had already been proposed in the previous European programs VELA [4] and NACRE [2], totally or partially dedicated to flying wings. The pressurized part of a flying wing, made up of a volume which upper (suction face) and lower sides (undersurface) are relatively flat, constitutes the most unfavorable configuration in terms of structure behavior with respect to the compressive forces. In this area, the fuselage does not have a circular cross section, and the pressure cannot be only balanced by tensile stresses in the skins. In the absence of frames, the upper and lower skins will be subjected to bending moments, and thus to very important stress gradients through the thickness. The main issue of this configuration is that it is necessary to stiffen the skin in order to limit, as much as possible, the flexural strains (and consequently the stresses) to minimize the mass. By order of decreasing importance, the three types of loading which induce bending moments on the fuselage skins are:

- the cabin pressurization,
- the transmission of a part of the bending moment from one wing to the other (along the Y axis), the other part being transmitted by nonpressurized rear part of the fuselage,

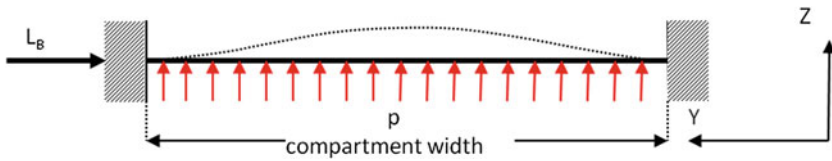


Fig. 3.24 Loads acting on the fuselage upper skin

- and the transmission, along the fuselage (according to direction X), of the bending moment induced by the weight of the aircraft structure as well as freight and passengers.

The first and the third load cases all concern the cabin, while the second concerns, approximately, the part of the fuselage located between the wing roots.

If one considers the cabin separation walls as nondeformable (in fact there are slightly extended in traction), the upper side and lower side can be modeled (Fig. 3.24) as flat panels clamped at their two ends. One of the two supports is fixed (on the level of the symmetry plane XOZ of the fuselage), the other is movable.

The inner side of the skin is subjected to the cabin pressure p , since on one of the embeddings one has a tensile force L_B or a compression force, induced by the bending moment M_B passing through the central part of the fuselage and due to the aerodynamic lifting force acting on the wings.

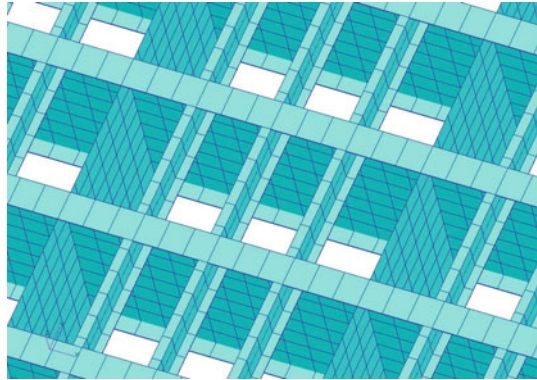
3.3.5.2 Configuration

In this configuration, it is obvious that a skin of a few millimeters thickness will be unable to support these loads. The proposed single shell concept should support the skin with transverse frames (I cross-section beams) lying in the direction Y . These frames are in theory sufficient to support compression and tensile stresses induced by the cabin pressurization acting on the skins. They support also the tensile (or compression) stresses due to the side forces L_B .

The bending moment supported by the transverse frames being very important, the frame pitch is considerable smaller (about half) in X direction than in Y direction. However, these frames are not able to support the bending moment along the X axis, due to the weight of the aircraft. For this reason, it is also necessary to put frames in the X direction. To avoid skin buckling, it would then be necessary to put stringers on the inner skin side in the X direction.

The transverse and longitudinal frames constitute a kind of grid of the fuselage structure which is able to support at the same time the cabin pressure as well as the bending moments due to the lifting loads and the aircraft weight. The skins, lying on a frame network, can then be locally considered as plates embedded on their circumference. Since the frames support the bending moments as well as the lateral compression load, the skin can then have a small thickness. However, in order to avoid a too large deflection of the skin panels located between each frame under the

Fig. 3.25 Skin stringers layout within the supporting grid



action cabin pressurization, it is also necessary to put stringers on the inner skin side. Three stringers were laid out according to Fig. 3.25.

3.3.5.3 Finite Element Modeling of a Fuselage Portion

After having described the basic fuselage structure as well as the principles which guided the technological choices, it is necessary to check, in detail, if the design solutions are relevant from a mechanical point of view, and if they lead to a light-weight concept. For this purpose, the single shell structure has been modeled by finite elements to check the structural behavior under cabin pressurization and buckling.

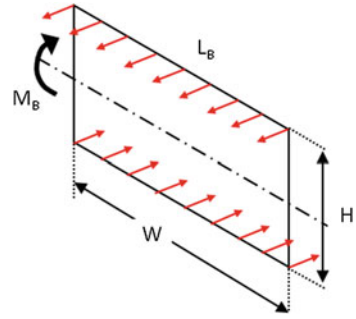
A representative flat portion of the fuselage has been considered. It contains 13 transverse frames along the X axis and 8 longitudinal frames along the Y axis. The skins and the frames were meshed with 4 node quadratic elements (Q4 linear interpolation), while the frame flanges as well as the stringers were meshed with beam elements. This mesh is sufficiently refined to calculate the local displacements and deflections to show the stress concentrations and to perform buckling calculation with confident results. The boundary conditions consist of clamping (blocking of Y displacements) on one side, a blocking of vertical displacements (according to Z) on the longitudinal frames. In this area, the frames can be considered as embedded on one side, but free to move in the transverse direction on the opposite side, due to the lateral load L_B , a blocking of displacements along X on both the transverse frame ends.

The materials used to manufacture the different components are:

- for the skins: quasi-isotropic carbon-fiber-reinforced polymer (CFRP) laminate
- for the longitudinal and transverse frames: orthotropic CFRP laminate
- and for the stringers: orthotropic CFRP laminate.

The cabin pressurization $p = 0.7$ bar (see Sect. 3.3.4.1) and the lateral load L_B have been taken into account. This load depends on the bending moment due to the

Fig. 3.26 Membrane loads acting on fuselage skin



aerodynamic pressure distribution discussed in Sect. 2.4. The most adverse loading Case A has been applied by integrating the respective pressure distribution.

According to the diagram of Fig. 3.26, one can estimate the lineic compression load L_B in the following way. If we assume that only the lower and upper skins of the fuselage support the bending moment, one can then write that:

$$L_B = \frac{M_B}{HW} \quad (3.13)$$

where W and H respectively represent the equivalent width of the fuselage involved in the transmission of the bending moment and the distance between the two skins. A mean value of L_B equal to approximately 500 kN/m was calculated.

The first calculation checked the stresses induced by the cabin pressurization only. Figure 3.27 shows the map of the displacement field calculated by FEM, where it is clearly visible that displacements result from the superposition of a global displacement due to the transverse frame deflection, and a local skin deflection, limited to small values because of the stringer stiffness. The mean skin waviness amplitude does not exceed 20 mm, which should not deteriorate the air flow around the fuselage, and thus the aerodynamic performances. Strain distributions in the skins and the frames have been checked. It can be noted that the maximum strain does not exceed 0.2 %, which largely satisfies the allowable strain criterion in Sect. 3.3.3.1. The longitudinal frames are strained at a very low level.

In the overall weight estimation, the transverse frames have the most significant weight contribution, because they mainly support the bending moments. Overall, a total specific weight of 21 kg/m² was estimated for the design.

In addition to the pressure cabin loading case, we added a lateral compression load $L_B = 500$ kN/m to check the buckling behavior of this fuselage portion. We chose a nonlinear elastic calculation method, giving results closer to reality. This calculation consists of application of load increments and to evaluate the tangent stiffness matrix at each iteration. For the initial concept, the buckling load is equal to approximately 25 % of the ultimate load. This small value was mainly due to the local buckling of the transverse and longitudinal frame flanges. It has been decided to put stiffeners on the longitudinal frames, and to reinforce the lower parts of the transverse frames with

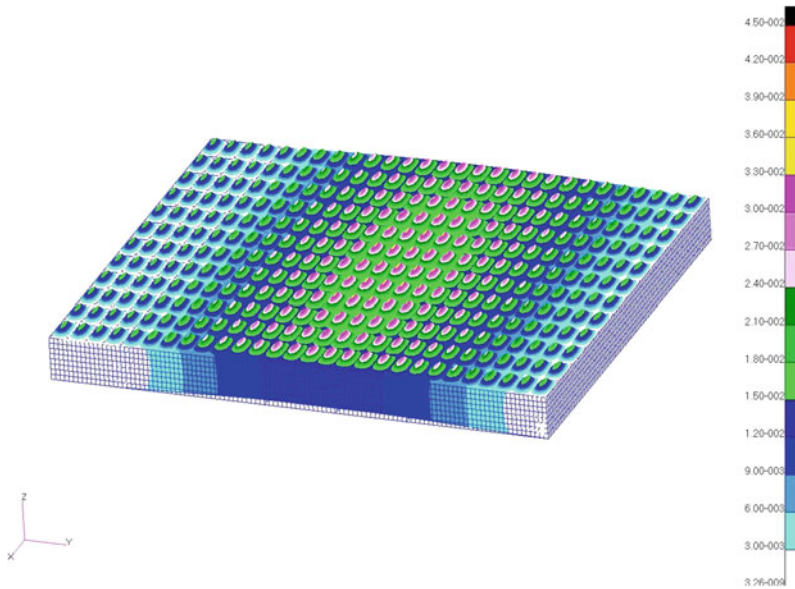


Fig. 3.27 Displacement field (*left scale* in m) calculated for cabin pressure only

cross-section beams. The frames were also reinforced by using a sandwich structure to increase the flexural inertia in the transverse direction. Since the transverse flexural stiffness of the frames plays a central role, it is preferable to reinforce them by a kind of stringer, rather than to increase the web thickness. For this reason, the thickness of the transverse frames was not modified.

The thickness of the skin was changed, and this modified structure supports the combined effect of the cabin pressurization and the lateral compression load. In fact, L_B has a stiffening effect on the frames, and the global displacement is smaller than that obtained for the cabin pressurization only. The mass per unit area increases from 21 to 23 kg/m². The cabin will thus be reinforced in this way to resist at the same time to the internal pressurization, to the compression load induced by the bending moment due to the wings, but also to the bending moment due to aircraft own weight and payload (along axis X). As for the wing, we will use an equivalent material with specific properties for membrane/flexion coupling.

3.3.5.4 Cabin Lateral Bulkheads

Around the cabin, the forces induced by cabin pressurization are supported by three convex walls located:

- at the fuselage leading edge (CB1),
- between the cabin and the transition area (CB2),
- at the rear cabin bulkhead (CB3).

In the optimal case, these walls should have a semi-cylindrical shape, in order to balance the cabin pressure by tensile stresses, to minimize the wall deformation as well as its thickness and mass. This constitutes the ideal case which, in fact, is only satisfied for CB3 since it is not possible to design a semicircular wall when:

- the external shape is imposed, as for the leading edge of cabin (CB1), by the aerodynamic shape of the airfoil,
- there is a strong variation of the external shape, as in the transition area.

In those cases, the wall can have only an elliptic shape which main dimensions ($b/h < 1$) are imposed by the tangency conditions with the other surfaces. Indeed, when the b/h ratio decreases, it is necessary to increase the wall thickness to maintain the strains below the allowable level, which leads to an increase in the mass. The addition of stiffeners on the wall skin (I cross-section shape) makes it possible to reduce the strains, by limiting the deflection, and thus to minimize the mass. This is the solution adopted in the fuselage concept to stiffen the bulkheads CB1 and CB2, but also CB3. Although in the rear bulkhead CB3, the shape is already semicircular, stiffeners were added to improve the elastic stability of the bulkhead regarding to local buckling.

3.3.5.5 Passengers Floor

The passengers floor (Fig. 3.28) is manufactured with composite material transverse beams (along Y axis) connected by some longitudinal beams of the same size. These beams confer floor flexural stiffness, and support another set of beams of smaller section along the X axis, with a small pitch to be able to fix the passenger seat rails. The largest beams are connected to the cabin separation walls as well as the cabin bulkheads by lattices made up of circular cross-section rods connected to the X and Y frames. There are two kinds of lattices: those laid out in vertical plane to attach

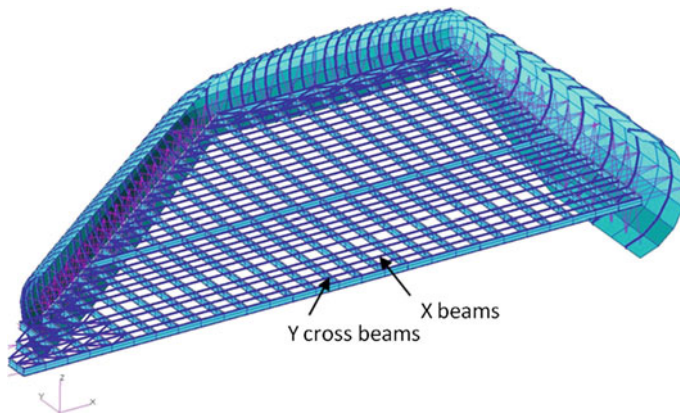


Fig. 3.28 Passengers floor mesh and construction

the cabin floor to the cabin structure, and those arranged on a horizontal plane to attach the passenger floor to the bulkheads to avoid large lateral displacements. This lattice consists of parallel rods connected to each other by rods laid out in diagonal (Fig. 3.28) to support the shear forces.

3.3.5.6 Transition Area

The transition area is a more complex structure subjected to high loads, since the bending moment is transmitted from the wing to the fuselage, as well as the shear forces. Figure 3.29 shows two views of the FE mesh to distinguish the main components:

- the skins (on top left of Fig. 3.29),
- the four spars: the first (S1) connecting the cabin leading edge spar, and the third one (S3) connecting the trailing edge spar to the rear fuselage spar,
- stiffeners laid out between the spars on the skin sides and connecting the wing box to the fuselage Y frames.

The four spars are reinforced by flanges (not shown in Fig. 3.29) extended to the wing.

3.3.5.7 Rear Fuselage

The rear fuselage part, although not pressurized, has to support the engines, the aerodynamic pressure loads, and the forces at the flap hinges. It also transmits a fraction of the wing bending moment, because the last spar of the transition area is attached to one of the two transverse frames. The structure is conventional in the sense that it consists of two spars connected with ribs, on which lie the skins. In this manner, the structure is designed as a nondeformable box. However, spars,

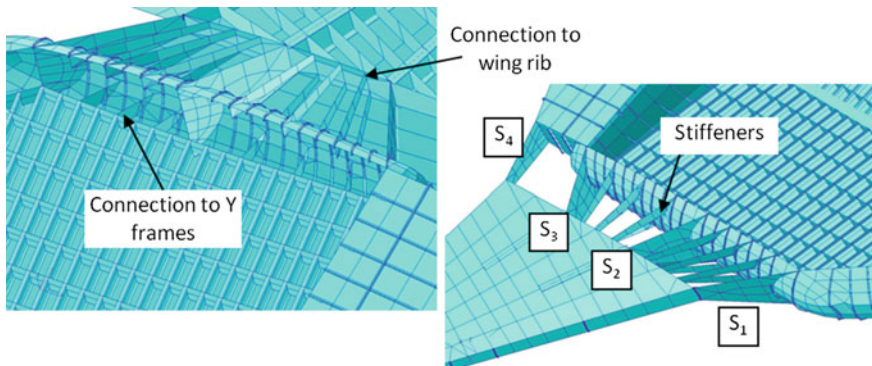


Fig. 3.29 Transition area structure

ribs, and skins are thin, and the risk of buckling is avoided by laying stiffeners on these components. To simplify the FE model, the engine mast is modeled with beam elements connected to one of the spars, and the engine is represented by a mass point.

3.3.5.8 Wing

The wing can be divided in three zones (Fig. 3.30) called W_1 , W_2 , and W_a . The two first are related to the wing itself, while the last one is related to the reinforcement of the wing tip in the vicinity of the winglet. The structure contains four spars in W_1 part and three in W_2 , ribs as well as skins (not shown in Fig. 3.30). The skins and the spars are subjected to compression and tensile stresses due to the bending moment, while the ribs ensure the elastic stability of the skins with respect to global buckling. Between two consecutive ribs, the skins are reinforced by stringers to avoid local buckling.

The rib pitch p_R has been determined by the following empirical rule:

$$p_R = 0.8\sqrt{t_A} \quad (3.14)$$

where t_A is the airfoil thickness. Since the airfoil chord (and consequently the thickness) decreases from the wing root toward the wing tip, p_R decreases also along the span Y_L . In order to build the wing mesh in a simple way, the rib pitch is varied by steps of decreasing values.

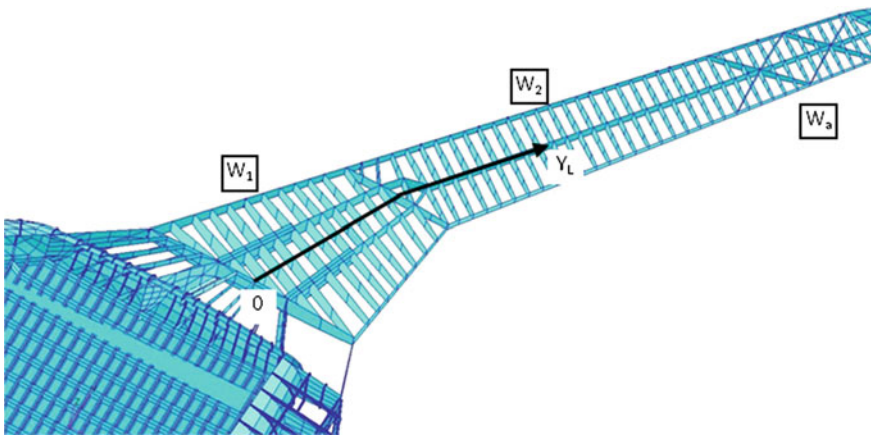


Fig. 3.30 Wing structure

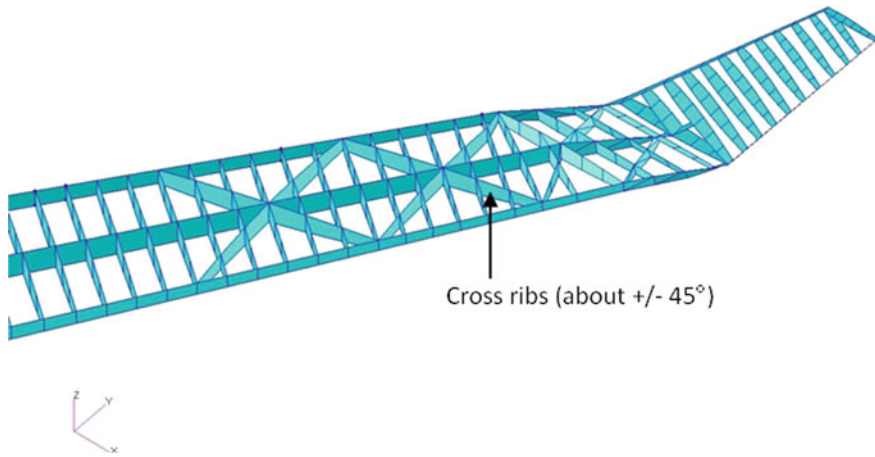


Fig. 3.31 Winglet structure

3.3.5.9 Winglet

The winglet has the same structure as the wing, except that there are two spars instead of three (Fig. 3.31). Preliminary flutter analyses revealed a too great flexibility in torsion of the wing area W_a . Consequently, this area was reinforced by cross ribs laid out at angles equal to more or less 45° to the spar direction. The flutter calculations moreover showed that the mass of the winglet was also important, and that its size had to be reduced.

3.3.5.10 Flaps and Slats

In order to simplify the FE model, which has to be sufficiently representative of the real structure behavior (in particular for flap modes), the slats and the flaps were modeled with plate elements (Fig. 3.32), in accordance with the geometrical data of Chap. 2, namely:

- 4 slats (1–4) attached on the wing box,
- 4 flaps (4–7) attached to the wing box, and
- 3 flaps (1–3) attached to the rear fuselage.

The structure of each flap consists of two skins assembled on spars and ribs. A flap is articulated on the wing trailing edge with several hinges and is actuated by jacks. The jacks (2 per flap) and the hinges (3 per flap) were modeled with beam elements on which stiffness and mass were allocated. The hinge and jack masses were determined by analytical formulations and were distributed on the flaps. Figure 3.51 shows a flap cross section and one can consider, at first approximation, that the two skins constitute an isosceles triangle. From the trailing edge spar heights h_1 and h_2 corresponding to the flap span beginning and end positions, we determined the

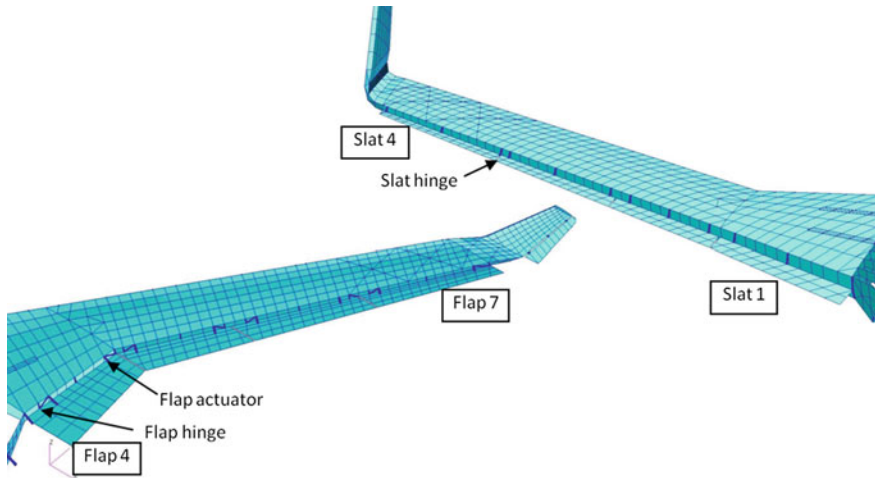


Fig. 3.32 Slats and flaps FE modeling

average height h of this flap as well as the average heights H_m (Fig. 3.33), such that:

$$h = \frac{h_1 + h_2}{2}; \quad H_{m1} = \frac{5}{6}h; \quad H_{m2} = \frac{1}{2}h; \quad H_{m3} = \frac{1}{3}h \quad (3.15)$$

In order to take into account a decreasing flexural stiffness, the flaps were divided into three elements along the chord c . Each element consists of two skins of same thickness e , parallels between them with a distance H_{m1} , H_{m2} , and H_{m3} according to their position in chord. In the FE model, a plate element is thus affected with a thickness $2e$, and its inertia I_1 per unit of width has a value:

$$I_1 = \frac{(2e)^3}{12} \quad (3.16)$$

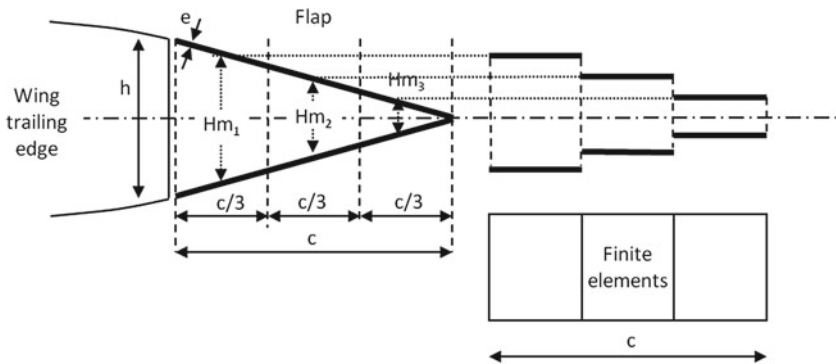


Fig. 3.33 Equivalent flap stiffness scheme

In fact, the real inertia I_2 of the plate element is:

$$I_2 = 2e \left(\frac{H_m}{2} \right)^2 \quad (3.17)$$

In the Nastran plate element properties card we affected a multiplying coefficient R for the inertia of each element, in function of its position in chord such as:

$$R = \frac{I_2}{I_1} = \frac{2H_m^2}{e^3} \quad (3.18)$$

The material considered is a quasi-isotropic composite laminate. Since inertia depends primarily on the skins, only the skins were taken into account in the calculation of R .

3.3.6 Nonstructural Masses

The FE model automatically takes into account the mass of each element, through the dimensions and the density of the material (see Sect. 3.3.3.1). However, it is also necessary to incorporate the nonstructural masses.

3.3.6.1 Fuel Tanks

Among all these masses, the fuel ($\rho = 803 \text{ kg/m}^3$) represents the most important part, and is distributed as follows (Fig. 3.34):

- Wing tank 1: 13,500 kg
- Wing tank 2: 5,150 kg
- Wing tank 3: 4,750 kg
- Center tank: 35,300 kg.

For each tank, the masses were assigned uniformly on the tank projected area, connected to the eight nodes located at the corners of each subtank (the displacement of each node of the structure is related to the displacement of the mass node).

In this model, we considered a full fuel center tank located in the fuselage area indicated in Fig. 3.35, that is, below the passengers floor and over the X and Y frames of the fuselage primary structure.

As proposed by Airbus, this tank will be probably used to adjust the aircraft CG and will not be uniformly filled over its entire length. This procedure allows to adjust the CG position X_g (compared to origin 0 of Fig. 3.35) by variation of the filling length X_m .

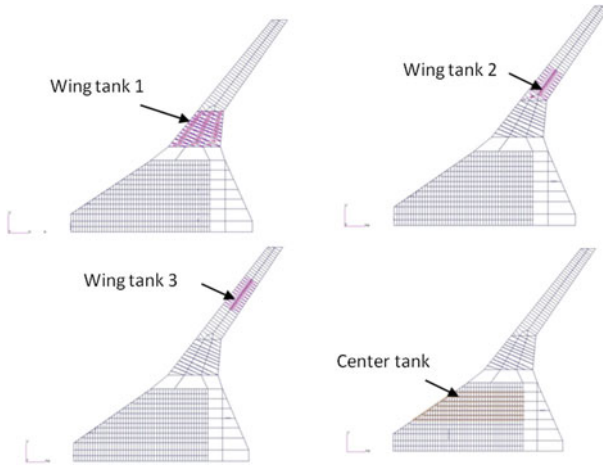
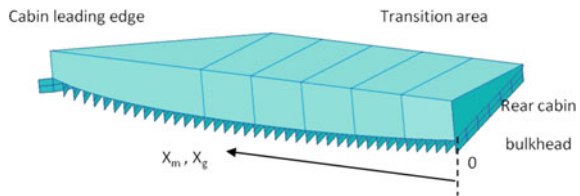


Fig. 3.34 Fuel tanks mass distribution on the BWB FE model

Fig. 3.35 Center fuel tank geometry



3.3.6.2 Flaps, Slats and Landing Gears

Due to the size of the flaps located at the rear fuselage and the loads they have to support, their mass per unit area is higher than those of the flaps located on the wing trailing edge. Within the framework of the previous European Commission (EC) program NACRE task 3.2, concerning the engine integration at the rear of a flying wing, these flaps have been suitably meshed. From this work, a realistic value has been estimated for this unconventional flap.

The mass of the landing gear was assigned in the same way as for the fuel tanks. The masses were distributed uniformly over the projected area of the bays and on the lower side skin of the fuselage. To preserve the simplicity of the model, the landing gear boxes were not meshed, although they probably represent a certain mass penalty (Fig. 3.36).

3.3.6.3 Equipments

The masses of the equipments have been grouped into three categories:

- navigation and communication: 900 kg
- electric systems and furnishings: 9,685 kg
- operating items: 17,710 kg.

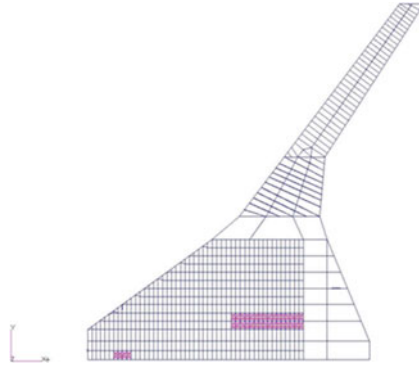


Fig. 3.36 Landing gears mass distribution on the BWB FE model

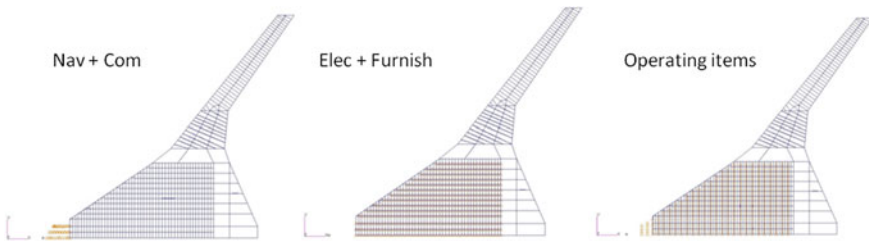


Fig. 3.37 Equipment mass distribution on the BWB FE model

These values were obtained by gathering the various mass items provided by TUM. Their assignment has been done in the same way as explained before (Fig. 3.37).

3.3.6.4 Freight and Passengers

The mass assignment is shown in Fig. 3.38. Freight as well as passengers masses were evaluated as 7,200 and 19,100 kg, respectively.

3.3.7 Finite Element Calculation

3.3.7.1 Mesh

Only one half of the aircraft has been meshed (Fig. 3.39), and the mesh is composed of the following elements (with linear displacement interpolation):

- CQUAD4: quadrangular plate elements
- TRIA3: triangular plate elements

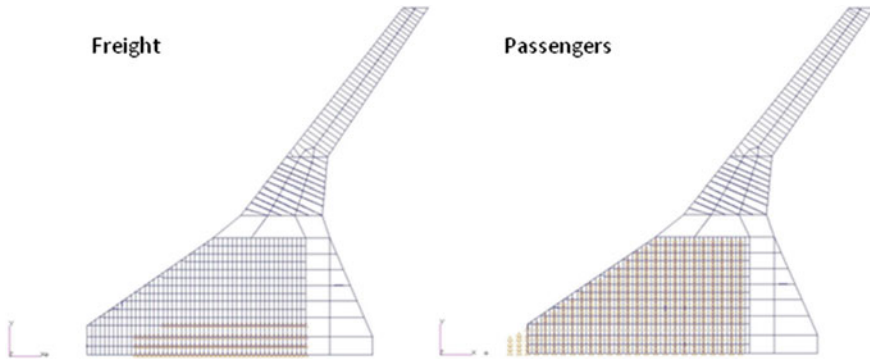


Fig. 3.38 Freight and passengers mass distribution on the BWB FE model

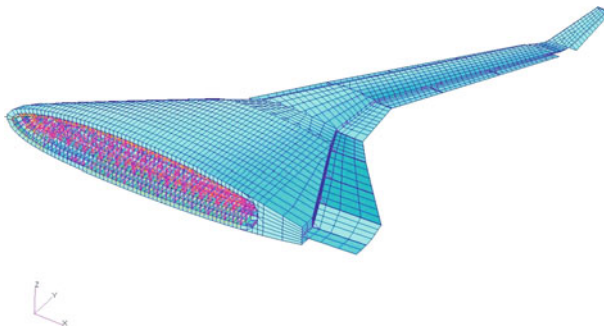


Fig. 3.39 Complete FE model of the half-BWB

- CBAR: beam element
- CROD: rod elements (tensile/compression force along rod axis only).

The total number of nodes and elements are equal to about 11,800 and 23,000 respectively. The structure has been meshed with PATRAN software and the FE calculations were performed with NASTRAN (MSC Software).

3.3.7.2 Loads and Boundary Conditions

For the static calculations, the loading cases of Table 3.2 were applied to the model. The boundary conditions consisted in blocking in the mid plane ($Y = 0$):

- all the displacements in the Y direction for the nodes located in this plane (loading symmetry condition),
- displacements in the Z direction for the nodes located at the two ends of the fuselage,

- and some displacements in the X directions for the nodes located in the vicinity of the cockpit.

3.3.7.3 Strain Analysis Procedure

For each loading case, it was evaluated that the strains supported by the different structural components did not exceed the allowable values of Table 3.2. Consider loading Case D, for which the allowable strain should not exceed 0.5 %. Let the principal strains calculated at the center of each element number i ($i = 1, \dots, N$) of a given structural component (for example, the lower fuselage skin), N being the number of elements of this component. For each element i , one takes only into account the maximum value of the principal strain, such as:

$$\varepsilon^i = \max(\varepsilon_{\text{I}}^i, \varepsilon_{\text{II}}^i), \quad (3.19)$$

$\varepsilon_{\text{I}}^i, \varepsilon_{\text{II}}^i$ being the principal strains.

For each element having an area S_i , the couples (S^i, ε^i) are ranked by increasing strain values, such as:

$$\varepsilon^i < \varepsilon^{i+1} \quad (3.20)$$

The associated probability is then evaluated with the following relationship:

$$P^i = \frac{\sum_{j=1}^i S^j}{\sum_{j=1}^N S^j}, \quad (3.21)$$

the denominator representing the area of the component. In this way, one obtains the fraction of the component area for which the strain is smaller than a given value ε^i . The graph of Fig. 3.40 shows the strain distribution function for the lower fuselage skin calculated for the loading Case D of Table 3.2.

From Fig. 3.40, it is obvious that 60 % of the skin area is subjected to a strain lower than about 0.2 %, and that the whole component is not subjected to strains higher than 0.5 %. The strain criterion (1) is thus satisfied. From the distribution of Fig. 3.40, the strains at different area percentages have been extracted for the loading Case D. As a matter of fact, more than 99 % of the skin area is subjected to strains lower than 0.47 %, and that only 1 % exceeds the limit strain of 0.5 %.

In this kind of analysis, it is necessary to keep in mind that the FE model is the result of a preliminary design approach, so all the parts of a given component are not obliged to be under the allowable value. For example, one can tolerate that 5 % (even 10 %) of the component area will be above the allowable value, because generally a large fraction of the component will be subjected to very small strains. Since the

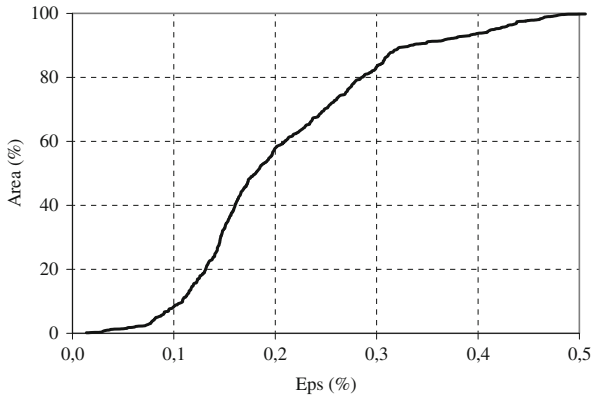


Fig. 3.40 Max strain distribution calculated for the upper skin and load case D

thickness was set to a constant value for a structural component, the mass surplus of the less strained areas could be reallocated to the higher strained areas, which leads to a mass redistribution without global mass variation.

3.3.7.4 Static Calculation Results

To illustrate the preceding step, the graph of Fig. 3.41 clearly highlights that in most of the components, 95 % of their area is under the allowable strain of 0.34 %. Some components should therefore be reinforced, but within the framework of this project and regarding the small percentages concerned by higher strains, this is more relevant for a detailed design.

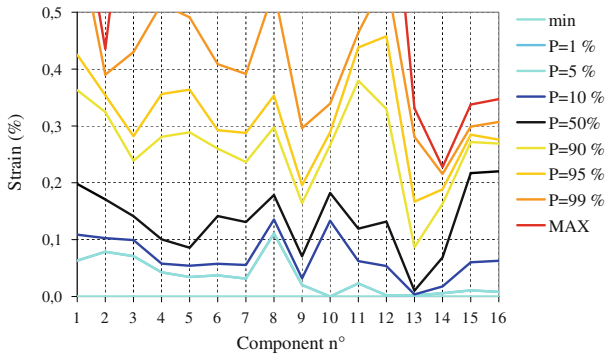


Fig. 3.41 Max strain distribution functions for the different fuselage parts for load Cases A, B, and C

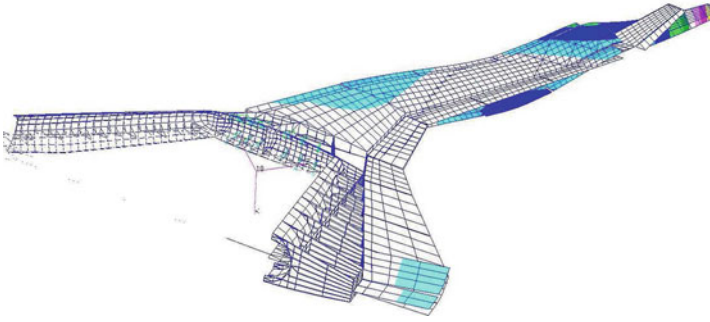


Fig. 3.42 An example of superimposition of global and local modes ($f = 8.8$ Hz)

3.3.7.5 Modal Analysis Results

Modal analysis has been performed under NASTRAN to check if there were no local modes which could lead to a more complicated flutter analysis. During this task, several analyses were performed, especially for the cabin floor, which was reinforced to eliminate most of the local modes. The first wing bending mode comes to lie at 1.16 Hz. Bending and torsion modes of the wing can be easily identified since they are not coupled. But at higher frequencies, some local modes can appear as shown in Fig. 3.42. The shown mode is a result of a superposition of a global wing mode and a local flap mode.

The first passenger floor mode is over 10 Hz, which is in agreement with the recommendations of the ACFA team. Since one of the goals of this project is to study the influence of the aircraft aeroelastic behavior on the passenger comfort, floor stiffness properties have also to be set by the following design tasks. This will be easily done in the FE model, where the main components are set in different element groups which can be clearly and quickly identified.

3.3.8 Mass Estimation

3.3.8.1 Weight Breakdown

Table 3.3 summarizes the weights estimated for the different aircraft configurations. It gives the weight breakdown of the BWB primary structure calculated from the FE model. This table includes some values estimated by TUM such as the engine and the landing gears.

MTOW and MZFW are respectively equal to 391 and 273 tons. These values can be compared to the values taken into account to determine the loading cases of Sect. 3.3.4, which were equal to 400 and 302 tons respectively. The calculation

Table 3.3 Weight summary for the half and complete BWB

Item	Item weight (kg)	Total (kg)
Structure	164,292	164,292
Equipments	21,170	(MWE) 185,462
Ops items	35,420	(operating empty weight (OWE)) 220,882
Freight and pax	52,582	(MZFW) 273,464
Fuel	116,800	(MTOW) 390,864

carried out with the initial values in Sect. 3.3.4.2 is thus slightly conservative and the weight difference is acceptable.

3.3.8.2 Aircraft Mass and Inertia Properties

The values of the half aircraft inertias given by the FE model at the CG, in the reference frame (Sect. 3.3.2), are given in Table 3.4. The position of CG is quite the same between both configurations, although inertias vary much more significantly because of the full tanks.

3.3.9 Conclusion

The initial model has been modified many times to take into account the suggestions of the different partners. In accordance with the remarks of TUM, some parts of the structure were reinforced with respect to buckling, and the material properties have been updated according to the technological constraints induced by the manufacturing process. The flutter preliminary calculations showed that it was crucial to reinforce the winglet and the surrounding attachment area at the wing tip, and to reduce the winglet area. The updated model was finally delivered to the partners responsible for model analysis and reduction.

Table 3.4 Inertia of the complete BWB calculated at the aircraft CG in the reference frame

	MTOW	MZFW
<i>Inertia (kg m²)</i>		
XX	2.6224E+07	1.6127E+07
YY	3.0242E+07	2.4743E+07
ZZ	5.3114E+07	3.8209E+07
<i>CG location (m)</i>		
Xg	23.64	23.55

3.4 Aerodynamic Modeling

C. Breitsamter, M. Meyer, D. Paulus and T. Klimmek

Unconventional aircraft designs like BWB designs are a possible solution to achieve the ambitious economic and ecologic goals of future air transport systems to reduce the fuel consumption, CO₂-emissions by 50 % and the external noise by 4–5 dB. In previous project dealing with BWB configuration, like the EC-funded projects VELA (2002–2005) and NACRE (2005–2008), the high need for active control and related expertise has been identified. Since flight control design and flight performance are strongly influenced by the aircraft aerodynamics, it is inevitable to have accurate aerodynamic predictions even in the preliminary design process. Due to the strong nonlinear phenomena occurring on the BWB configuration, results of acceptable accuracy can only be obtained by high-fidelity simulations as opposed to simplified approaches, for example, empirical methods or linear aerodynamic methods without corrections. This section summarizes the aerodynamic computations carried out in task 2.2 of ACFA 2020. The goal is to provide a database of steady and unsteady aerodynamic data for task 2.3 that can be used for the setup of a reduced aerodynamic model in the frequency domain of the flight dynamics and the aeroelasticity of the ACFA BWB configuration. The data should cover the complete flight envelope, from low speed to cruise speed.

At first, the numerical methods used for the aerodynamic computations by the different partners, DLR-AE, FOI, NTUA, and TUM-AER, are explained with the focus on the fundamental concepts covering the flow physics.

3.4.1 Numerical Methods

In this subsection, the employed numerical methods are briefly described. Since potential flow methods are very robust and time efficient, they are the standard tools for aeroelastic simulations in industrial practice. Nevertheless, computational fluid dynamics (CFD) solvers provide much better accuracy in the transonic regime. Hence, several flow solvers based on different numerical methods are applied for the ACFA BWB configuration to provide the best fitted and most efficient solution approach according to different flight conditions. Furthermore, a comparison between independent flow solvers is valuable to assess the numerical results in lack of experimental data. DLR-AE used linear potential flow methods to predict the aerodynamic pressure distribution. FOI, NTUA, and TUM-AER solved the Euler equations, while FOI also conducted simulations based on the Reynolds-averaged Navier-Stokes (RANS) equations. The structured and unstructured meshes for solving the Euler equations were built with the commercial software ANSYS ICM-CFD by FOI. The meshes for the RANS equations were built using the unstructured Euler meshes and an FOI-in-house software TRITET based on an advancing front

algorithm in order to create a hybrid mesh of prismatic and tetrahedral elements. The generation of the deflected fluid surface grids according to the structural eigenmodes was done by FOI.

3.4.1.1 Potential Flow Methods

In order to cover the low-speed regime ($M = 0.2-0.6$), the commercial surface panel method VSAERO was used by DLR-AE. VSAERO solves the three-dimensional potential flow equations by the boundary integral method (panel method) based on Morinos formulation [7]. Viscous boundary layer effects are calculated by integral methods which include convergence/divergence terms along streamlines and are coupled to the potential flow solution by surface transpiration. Wake models for wing trailing edge separation, bluff-body and cross-flow separation are available. Matrix solutions are obtained by a variety of methods which include Direct, Blocked Gauss-Seidel, Banded Jacobi, and GMRES solvers. An option to VSAERO is to calculate the aerodynamics of a structure oscillating with a prescribed shape, amplitude, and frequency. So the steady and oscillatory pressures including the in-phase (real) and out-of-phase (imaginary) pressures are determined. Linear analysis is used to achieve calculation times equivalent to steady-state calculations. The unsteady pressures can be linearized about the freestream, or for greater accuracy, linearized from the steady-state solution. Aeroelastic calculations of divergence and flutter are possible by generating the aerodynamic influence coefficients suitable for calculating pressures on a body undergoing arbitrary oscillations. A structured, multi-block surface grid of the ACFA BWB configuration was generated for VSAERO. The mesh is depicted in Fig. 3.43. The potential flow model needs also a geometry description of the trailing wakes. They are attached to the trailing edges of the wing-body shape including the winglets. The mesh consists of 19,398 body panels and 6,482 wake panels. For Mach numbers higher than $M = 0.6$, VSAERO is hardly applicable, because of the presence of aerodynamic shocks which cannot be captured correctly by this method. The grids are locally refined in areas where flaps are located. By modifying the boundary condition for panels representing a flap, static computations for deflected flaps can be conducted efficiently without modifying the actual geometry. VSAERO was also used to calculate the dynamic derivatives.

3.4.1.2 CFD Methods

All aerodynamic simulations by FOI were carried out using the in-house CFD code EDGE [1]. EDGE is a parallelized CFD flow solver system for solving 2D/3D viscous/inviscid, compressible flow problems on unstructured grids with arbitrary elements. The flow solver employs an edge-based formulation which uses a node-centered finite volume technique to solve the governing equations. The control volumes are nonoverlapping and are formed by a dual grid, which is computed from the control surfaces for each edge of the primary input mesh. In the flow solver,

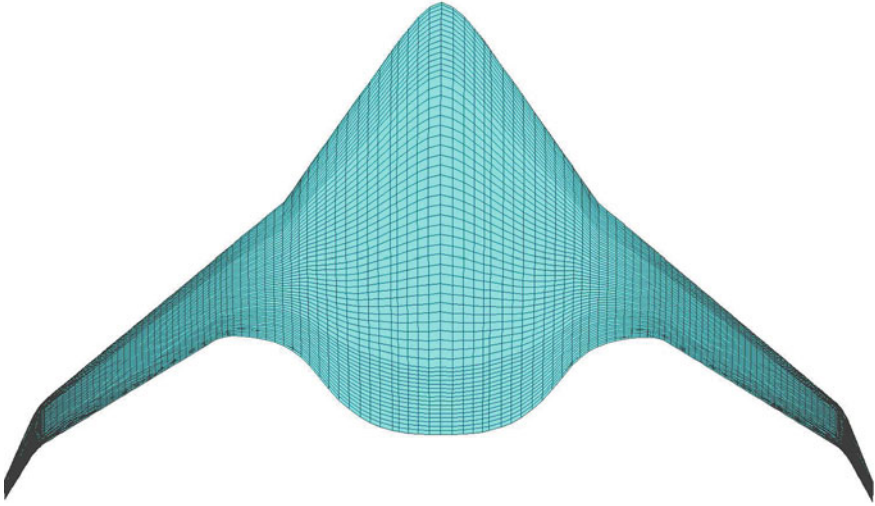


Fig. 3.43 Panel mesh by DLR-AE

the governing equations are integrated explicitly toward steady state with Runge-Kutta time integration. Convergence is accelerated using agglomeration multigrid and implicit residual smoothing. Time-accurate computations can be performed using a semi-implicit, dual time-stepping scheme which exploits convergence acceleration technique via a steady-state inner iteration procedure. EDGE solves the RANS compressible equations in either a steady frame of reference or in a frame with system rotation. Turbulence can be modeled with eddy viscosity models or explicit algebraic Reynolds stress models. Edge contains different spatial discretizations for the mean flow as well as the turbulence, different gas models, steady-state and time-accurate integration, low-speed preconditioning, etc. Applications include shape optimization and aeroelasticity. The used unstructured meshes comprise up to 1.37 million nodes for inviscid simulations and up to 12.2 million nodes for the viscous case. In Fig. 3.44, a surface mesh of the winglet is depicted.

In the TUM-AER flow solver AER-Eu, the Euler set of equations are discretized on structured finite volume grids [3]. The numerical convective fluxes are computed by the Roe scheme, and the diffusive fluxes are discretized by the Chakravarthy method. A total variation diminishing scheme prevents unphysical oscillations. For time advancement, the current calculations use a time-accurate scheme with lower-upper symmetric successive over relaxation (LU-SSOR). The numerical solver is second-order accurate in time and space. The AER-Eu has some special features. One is the ability to compute unsteady flows also forthright in the frequency domain, which guarantees high computational time efficiency in terms of CFD. It is based on a linear small disturbance approach applied to the Euler equations. Another feature is the extension to a Navier-Stokes set of equations in the AER-NS solver. With algebraic, 1- and 2-equation turbulence models RANS simulations can be carried out. These two features are not exploited in the ACFA 2020 project. However, an

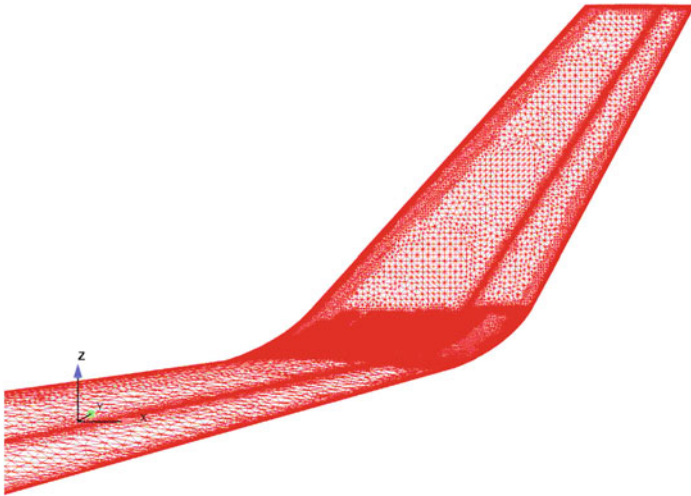


Fig. 3.44 Unstructured surface mesh at winglet by FOI

exploited feature is the ability to simulate deforming geometries. For calculations with deformed geometries, both deformed and undeformed spatial grids are required. The undeformed grid for the TUM-AER simulations was generated by TUM-AER in the commercial tool ANSYS ICEM-CFD and optimized by a TUM-AER in-house globally elliptic smoothing tool. This basic structured grid shows a favorable OO-block topology and consists of 1 million computational cells as depicted in Fig. 3.45. Domain extents are chosen such that farfield boundary conditions do not influence the flow physics near the aircraft. Grid independency was proven by grid convergence study. Besides the instantaneous and time-averaged aerodynamic derivatives, generalized aerodynamic forces (GAFs) are output of AER-Eu.

The NTUA flow solver is based on a vertex-centered finite volume scheme. The flow equations are cast in conservative form and integrated over finite volumes defined around the grid vertices. This solver may support unstructured or hybrid grids consisting of tetrahedra, hexahedra, pyramids, or prisms. The finite volumes are defined around each grid node, connecting the mass centers or circumcircles of the surrounding elements and the midnodes of the edges emanating from each node. For the given computational meshes, the second definition proved more efficient and, thus, is employed. Fluxes crossing the finite volume boundaries are all computed with second-order accuracy. The inviscid flux crossing the interface between the volumes centered at two adjacent nodes is computed by using the flux vector splitting scheme; second-order accuracy is obtained through variables extrapolation. The least squares method coupled with the Venkatakrisnan limiter was used for the reconstruction of the variables at the finite volumes interfaces. Dual (real and pseudo) time-stepping is employed. In the unsteady computations carried out, the computational mesh of each physical time step derives from the deformation of the previous real time step based on the selected mode or moving flap. The numerical solution of the discretized

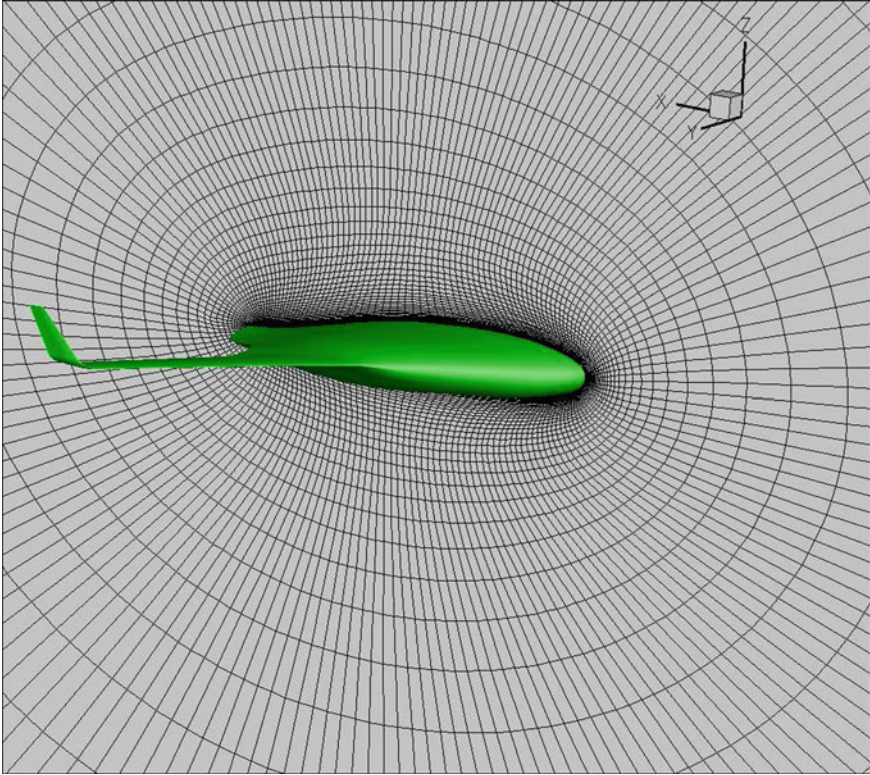


Fig. 3.45 Structured O-O-topology by TUM-AER

flow equations between two successive time steps is carried out by repetitively using the point implicit Jacobi method. The flow solver is fully parallelized, based on the multi-domain technique, and the PVM or MPI protocols. All the computations presented in this report have been carried out using the Euler equations solver.

3.4.1.3 Aeroelastic Coupling

Several procedures were tested for the fluid-structure coupling, especially procedures that do not require hand-selection of the nodes in the structural model in order to extrapolate the structure modal displacements to displacements of the CFD surface mesh. After several evaluations, the radial basis functions (RBF) were used for all computations. In the following, the eigenvectors or mode shapes, defined at the degrees of freedom of the FE model, are interpreted as deformations of the wetted surface, in terms of CFD mesh displacements. At first, the FE model and the CFD reference surface meshes were fitted to each other. The fluid mesh is translated and rotated so that leading and trailing edges in both grids fit each other. Denoting the

displacement vector by \mathbf{V} , the coupling between the structure and the fluid models is realized by

$$\mathbf{V}_{\text{CFD}} = \mathbf{H}\mathbf{V}_{\text{FEM}}. \quad (3.22)$$

The matrix \mathbf{H} represents the spline matrix and is computed by RBF. The aerodynamic forces \mathbf{F} acting on the structure and the fluid surface are also related by this spline matrix

$$\mathbf{F}_{\text{FEM}} = \mathbf{H}^T \mathbf{F}_{\text{CFD}}. \quad (3.23)$$

This formulation defines a conservative fluid-structure coupling, which can be shown by

$$\mathbf{V}_{\text{CFD}}^T \mathbf{F}_{\text{CFD}} = (\mathbf{H}\mathbf{V}_{\text{FEM}})^T \mathbf{F}_{\text{CFD}} = \mathbf{V}_{\text{FEM}}^T \mathbf{H}^T \mathbf{F}_{\text{CFD}} = \mathbf{V}_{\text{FEM}}^T \mathbf{F}_{\text{FEM}}. \quad (3.24)$$

The conservation of work is important for solving accurately aeroelastic problems. It guarantees that the GAFs computed by CFD are identical to the GAFs defined in the structure model. Unsteady aerodynamic methods can require scaling of the displacements in order to assure linear aerodynamic behavior and hence linear dependency of the GAFs with respect to the structural deformation. The CFD modes delivered by FOI were scaled such that the maximum displacement of each mode after scaling is 1/500 of the MAC. Finally, the GAFs Q due to harmonic oscillations in mode i and projected on mode j depend on the reduced frequency and are given by

$$Q_{ij} = \int_S c_{pi} \mathbf{V}_j d\mathbf{S}_i. \quad (3.25)$$

\mathbf{S} denotes the surface normal vector and c_p is the pressure coefficient.

3.4.2 Steady Simulation Results

The aim of this section is to give an overview of all computational results as well as a qualitative assessment of the data. Since experimental data are not available, a quantitative validation of the simulation results is not possible. But the results obtained by the different partners are compared. The next subsection deals with the assessment of the aerodynamic design based on steady simulation results.

3.4.2.1 Comparison of Numerical Models and Solvers

In terms of efficiency, the use of different flow models is common in aerodynamics because the relative viscosity, compressibility, and cross-flow effects vary with altitude and speed of the aircraft configuration. Different models are used in task 2.2 in order to build a database of aerodynamic data for the development of the flight control system.

In Fig. 3.46, global force and moment coefficients are plotted over the angle of attack for Mach numbers ranging from $M = 0.2$ to $M = 0.6$. Since no transonic flow effects are observed in this velocity range, steady-state results obtained by a RANS, using the Spalart-Almaras turbulence model, computed by FOI (FOI-R) are compared to semi-empirical results obtained with VSAERO (DLR-AE). Both models agree well regarding the lift coefficient. Differences appear for the drag and the pitching moment coefficient and vary with Mach number and angle of attack. The trend observed here is that results using VSAERO yield smaller absolute values

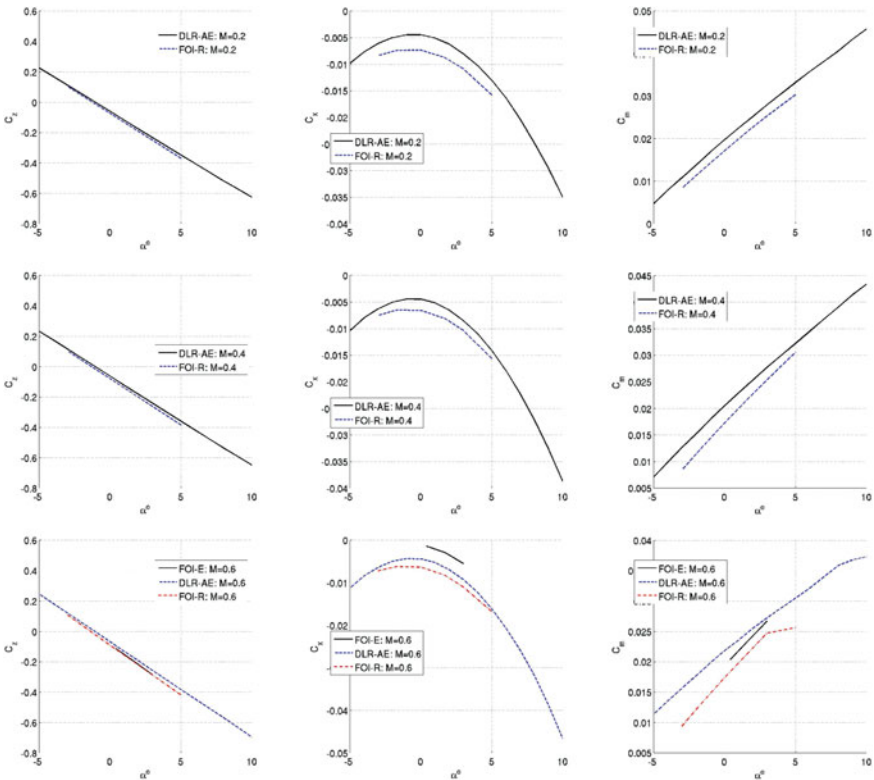


Fig. 3.46 Global force and moment coefficients for varying angle of attack and Mach number $M = 0.2-0.6$, DLR-AE (VSAERO), FOI-R (RANS), FOI-E (Euler)

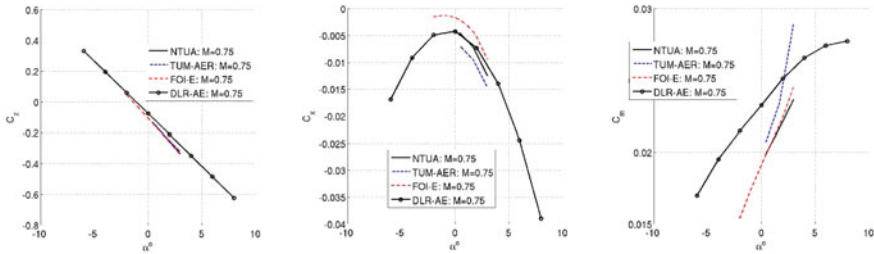


Fig. 3.47 Global force and moment coefficients for varying angle of attack and Mach number $M = 0.75$, DLR-AE (VSAERO), FOI-E (Euler), TUM-AER (Euler), NTUA (Euler)

than the simulations using the RANS solver in an interval of angles of attack from $\alpha = -4^\circ$ to 5° . The Mach number does not seem to influence these differences in the present velocity range.

Transonic effects become important for Mach numbers greater than 0.6 for this aircraft configuration. This can be observed in Fig. 3.47, especially in the moment coefficient. Since compressibility and three-dimensional effects cannot be represented accurately by VSAERO the deviations between the results increase. Differences in the results are not always caused by the simplifications made on the flow equations as for instance neglecting viscosity. There are also differences due to the numerical scheme used for solving the flow equations. The flow solvers used by FOI and NTUA use a vertex-centered finite volume scheme, whereas TUM-AER uses a finite volume discretization that is cell-centered. Both NTUA and TUM-AER used a Roe scheme with flux limiters whereas FOI used the second- and fourth-order artificial dissipation model (JST model). The comparison between NTUA, FOI-E, and TUM-AER indicates a good agreement on the lift force but also significant differences on the drag prediction, see Fig. 3.47. The drag obtained by the Euler solvers of TUM-AER and NTUA is considerably larger than the drag obtained by the Euler solver of FOI (FOI-E). This can be caused by the size of the fluid domain between the mesh built by FOI where the farfield boundary conditions are typically 50 chords away from the aircraft, whereas for TUM-AER the domain is much smaller.

In Fig. 3.48, the pressure coefficient distribution is given in four spanwise sections. Compared are inviscid simulation results provided by FOI, NTUA, and TUM-AER on meshes of different size. Effects of the mesh resolution are determined to be very small and hence the solution can be regarded as grid-converged. Discrepancies occur concerning the shock position, especially in the two outer sections. The shock position computed by FOI and TUM-AER agrees quite well, while NTUA predicts a shock located further downstream.

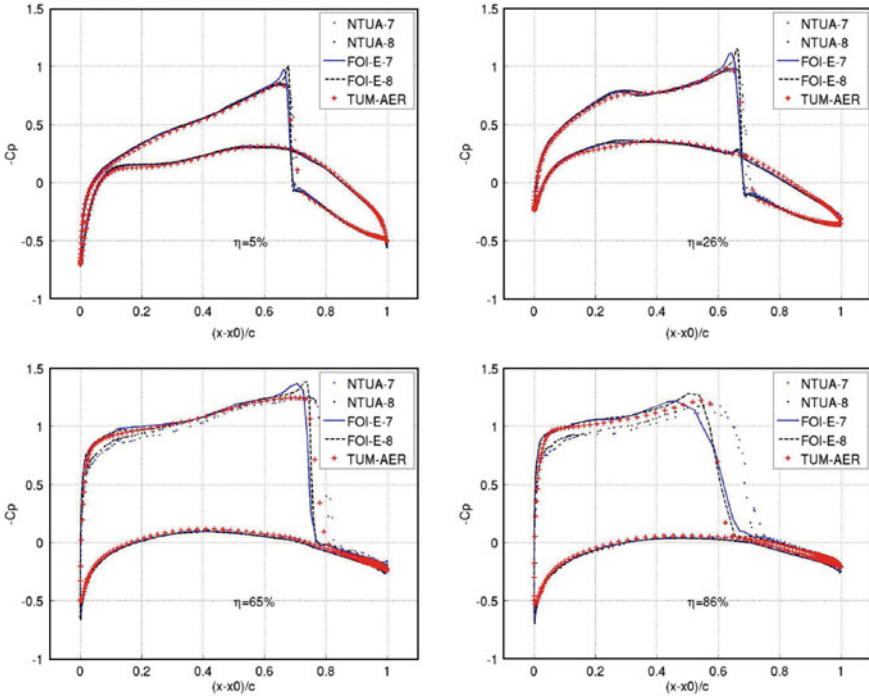


Fig. 3.48 Pressure coefficient distribution for $\alpha = 1.7^\circ$ and $M = 0.85$ at different spanwise locations η , FOI-E-7 (Euler, mesh coarse), FOI-E-8 (Euler, mesh fine), TUM-AER (Euler), NTUA-7 (Euler, mesh coarse), NTUA-8 (Euler, mesh fine)

3.4.2.2 Aerodynamic Design Analysis

The aerodynamics on the BWB aircraft are determined by strong nonlinear effects. A complex shock system is built up on the lower and upper part of the wing and the winglet at cruise conditions, shown in Fig. 3.49. With increasing Mach number, the shock system moves toward the trailing edge. The shock position differs strongly in spanwise direction. Hence, the strong shocks and the spanwise variation in shock locations affects markedly the aerodynamic performance, but the project was not aimed on a fully optimized transonic aerodynamic design.

Figure 3.50 shows the effect of the Mach number on the lift, drag, and the pitching moment coefficient. At higher Mach numbers, shock systems dominate the flow physics of the aircraft and thus the aerodynamic coefficients. Due to the shock system, the suction region on top of the wing becomes larger. This leads to a higher lift and higher drag coefficient. The total drag coefficient is mainly increased due to the contribution of the wave-drag. With increasing Mach number and angle of attack, respectively, the shock strength increases and the shock system moves toward the trailing edge of the wing leading also to a change in the pitching moment coefficient. This shock movement is also visible in the pressure coefficient plots at the two mid-

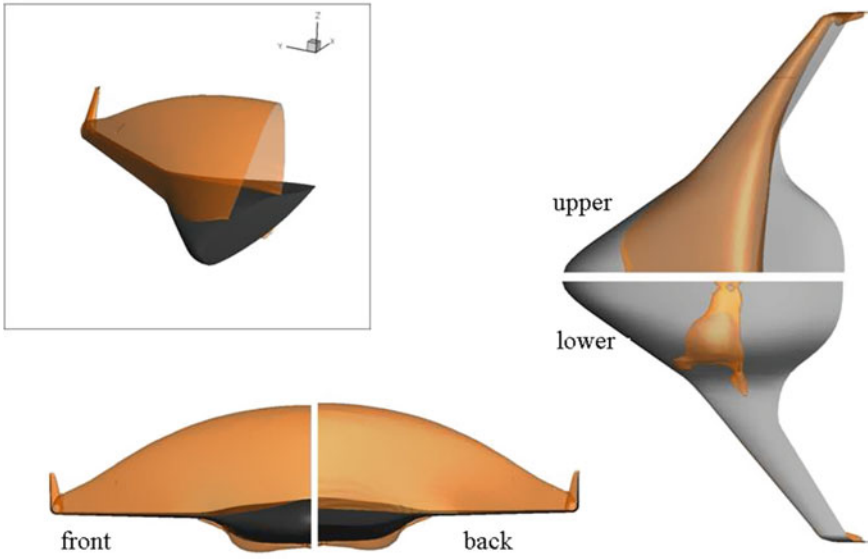


Fig. 3.49 Mach-isosurface ($M = 1$) for $M = 0.85$ and $\alpha = 1.7^\circ$, TUM-AER (Euler)

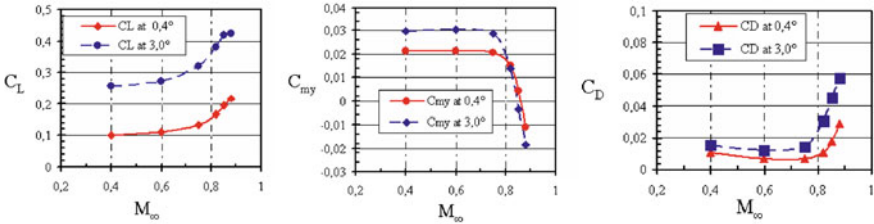


Fig. 3.50 Global force and moment coefficients for varying angle of attack and Mach number, TUM-AER (Euler)

flap positions in Fig. 3.51. The shock positions differ strongly in spanwise direction. Between $M = 0.85$ and $M = 0.88$, the shock position varies by 5% on the inner wing, while it varies by 15% on the outer wing. The respective shock strength shown by the pressure coefficient increase is 10% higher on the outer wing than on the inner wing. At $M = 0.75$, no shock occurs on the wing. A slightly smaller variation occurs for different angles of attack, see Fig. 3.52. The variation of the shock position implies an undesirable unequally distributed aerodynamic loading and has a direct influence on the aircraft handling qualities. Improvement can be achieved by a more suitable airfoil selection or by adapting the wing twist and wing sweep.

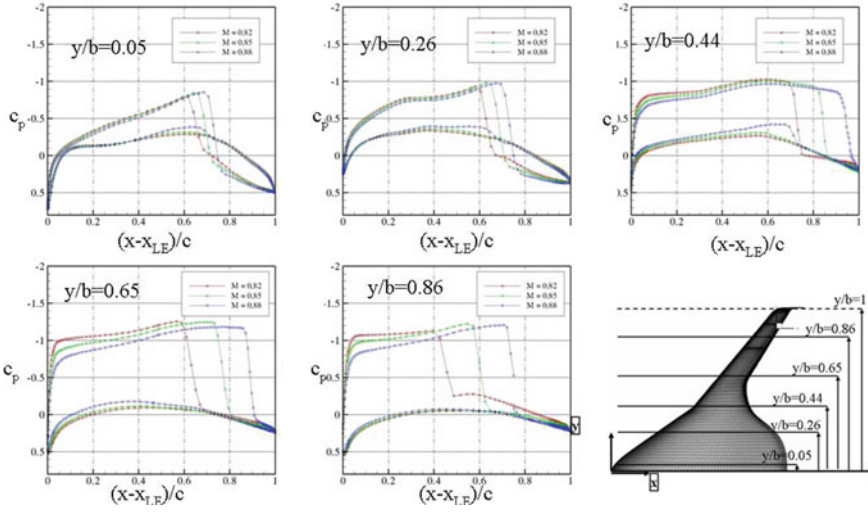


Fig. 3.51 Pressure coefficient distribution for $\alpha = 1.7^\circ$ and three Mach numbers at different spanwise locations η , TUM-AER (Euler)

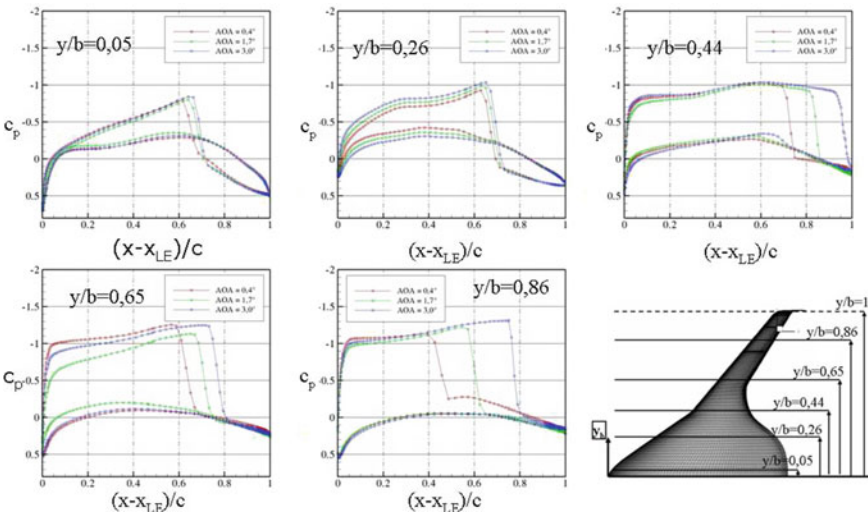


Fig. 3.52 Pressure coefficient distribution $M = 0.85$ and three angles of attack at different spanwise locations η , TUM-AER (Euler)

3.4.3 Unsteady Simulation Results

The steady simulations show that the Mach number has a significant influence on the aerodynamics and thus on the load distribution, particularly, on the outboard wing.

Therefore, the Mach number's influence for a wing bending mode at different reduced frequencies is investigated. The pressure coefficient's evolutions of the time-accurate simulations undergo a successive Fourier analysis. Figure 3.54 shows the real and imaginary parts of c_p for the previously used two mid-flap positions at two different Mach numbers and three different reduced frequencies for the bending mode. The pressure peaks indicate a shock position. The amplitude of the peak corresponds to the shock's strength and the width of the peak to the range of the shock movement due to the elastic bending motion. The three-dimensional bending motion can be considered as a plunge movement for a two-dimensional spanwise cut plane. The respective amplitude of the movement is higher on the outboard wing. The real part of c_p can be seen as quasi-stationary induced incidence α_0 locally at the deformation, while the imaginary part of c_p is due to the incidence α_i locally induced by the bending movement. The influence of the Mach number on both real and imaginary parts of c_p is larger on the suction side than on the lower side of the wing. Similar to the steady calculations, the c_p distribution on the outboard wing (at $y/b = 0.86$) is more susceptible to changes in the Mach number. At $M = 0.75$, the unsteady bending motion generates a double peak implying two recompression zones on the upper outboard wing close to the leading edge. A variation of the reduced frequency has also a higher impact on the c_p distribution along with the amplitude of the pressure peaks of the outboard wing. This is especially the case for the real part of c_p . For the imaginary part of c_p , a change in reduced frequency even leads to a local inversion in sign. However, this does not lead to global instabilities or to a respective change in sign of the global forces. To summarize, the c_p distribution, especially the one on the outboard wing, shows a very sensitive behavior to variations in Mach number and reduced frequency. These corresponding strong nonlinear phenomena can only be accounted for by the used high-fidelity simulations as opposed to simplified approaches based, for example, on potential theory.

In addition to the Euler computations, FOI carried out a number of viscous flow computations. Low Mach number computations with RANS allowed a more accurate comparison of the CFD results with VSAERO. Simulations with RANS at transonic Mach numbers ($M = 0.85$) complement the Euler CFD computations carried out by FOI (FOI-E), NTUA, and TUM-AER. The computations were carried out on two meshes, with different nodes densities, which allowed excluding grid convergence effects. All attempts at $M = 0.85$ were evident to suggest that the flow solution is unsteady. Therefore, for both grids, time-accurate solutions were computed. After passing the transient, the flow solutions converged to a harmonic flow regime oscillating at a frequency of $f = 0.7$ Hz, apparently driven by shock-boundary layer interaction. The left plot in Fig. 3.53 illustrates the transient toward the harmonic regime. The right plot shows the relation between drag and lift. The amplitude variations of the drag and lift coefficient measure about 10% of the absolute values.

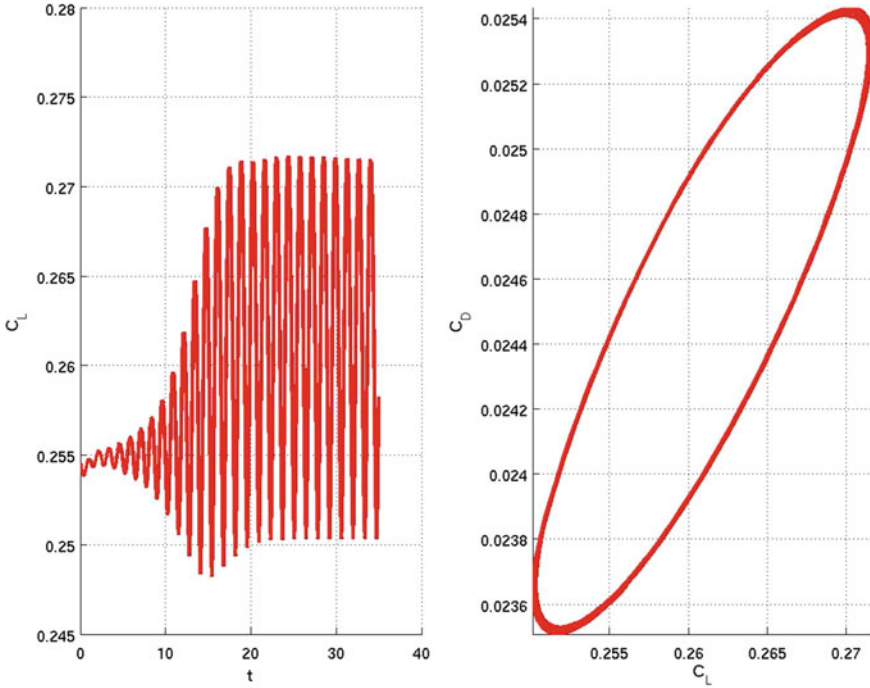


Fig. 3.53 Time-accurate computation of the lift and drag coefficient at $M = 0.85$ and $\alpha = 1.7^\circ$, FOI (RANS)

3.4.4 Conclusions

The aerodynamics of the ACFA blended wing body (BWB) based on a number of test cases comprising steady and unsteady results using potential theory and high-fidelity Euler/RANS simulations were analyzed. The results show that the pressure distribution and aerodynamic loads, respectively, are susceptible to changes in Mach number in the steady simulations as well as changes in Mach number or in reduced frequency in the unsteady simulations. Severe load distribution variations are especially located at the outboard wing. Furthermore, oscillations in the aerodynamic loads are observed at cruise conditions. For improvement, it is recommended to incorporate high-fidelity aerodynamic analysis and design methods already in the conceptual design phase. A comparison between panel and CFD methods showed pertinent agreement at Mach numbers $M < 0.6$. But strong nonlinear phenomena at higher Mach numbers can only be accounted for by the use of high-fidelity CFD simulations (Fig. 3.54).

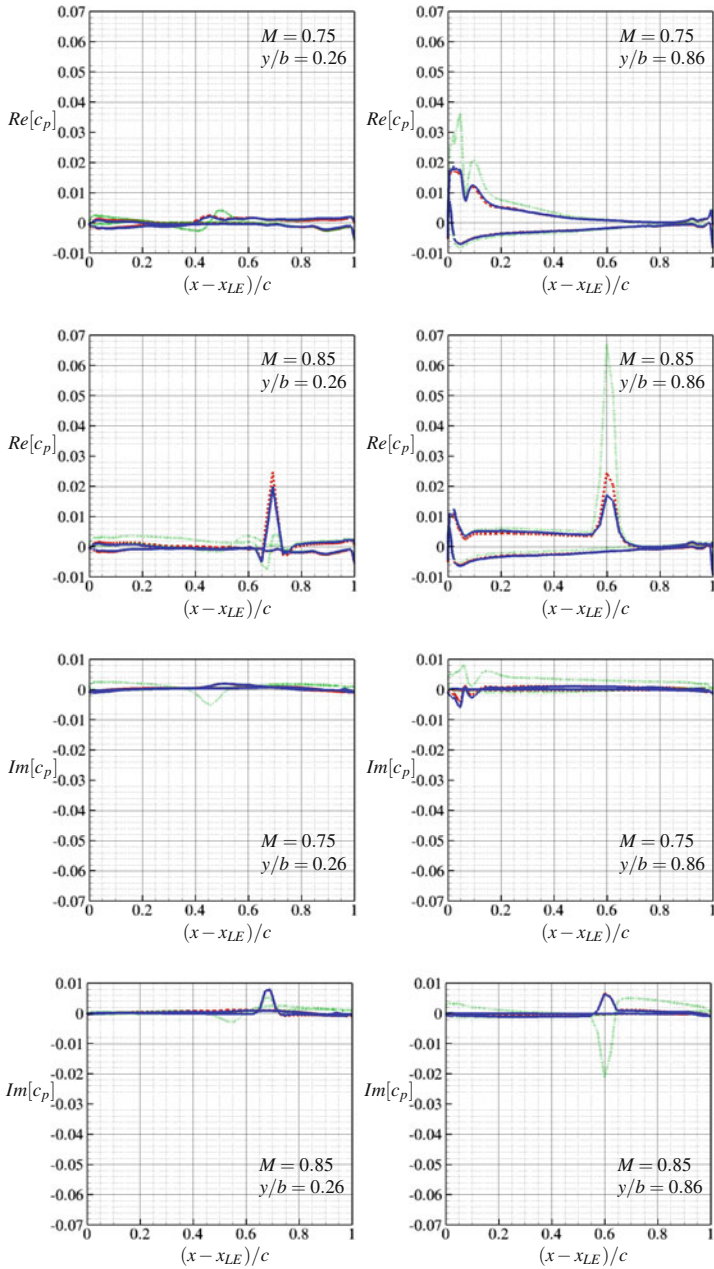


Fig. 3.54 Real and imaginary parts of the pressure coefficient, $Re[c_p]$ and $Im[c_p]$, in streamwise direction $(x - x_{LE})/c$ at different spanwise positions y/b for symmetric bending at different Mach numbers and $\alpha = 1.7^\circ$ (—: $k_{red} = 0.05$; - - : $k_{red} = 0.1$; ··· : $k_{red} = 0.5$)

3.5 Integrated Flight Dynamics and Aeroelastic Modeling

F. Stroscher and H. Baier

In the following, the modeling steps for the coupled flight dynamic and aeroelastic simulation model are described. The basis is the structural dynamic simulation model (Sect. 3.3) as well as the aerodynamic database (Sect. 3.4).

3.5.1 Structural Dynamics

Within the ACFA 2020 project, an FE model of the BWB aircraft primary structure was developed. The FE model level of detail is comparably low, but sufficient for the prediction of structural dynamic response in the considered frequency range. A full span model was applied in aeroelastic modeling, to directly take into account asymmetric turbulence excitation. The fuel tanks (Fig. 3.55) are represented by concentrated mass elements, rigidly connected to the structure.

The possible mass conditions of the aircraft are defined over the full range of fuel tank filling level, from empty to full. Further, the fuel distribution over tanks in wing and fuselage is considered, providing a useful margin of x -position of the aircraft center of gravity. Three configurations of fuel distributions are considered (CG1–3) for 11 steps of fuel filling (index 0 with 0 % filling to index 10 with 100 % filling), which yields 33 structural variants in total.

The natural modes for all mass configurations of the FE model are extracted by numerical solution of the vibration eigenvalue problem (3.26). Structural damping is neglected in this approach, resulting in noncomplex eigenvectors.

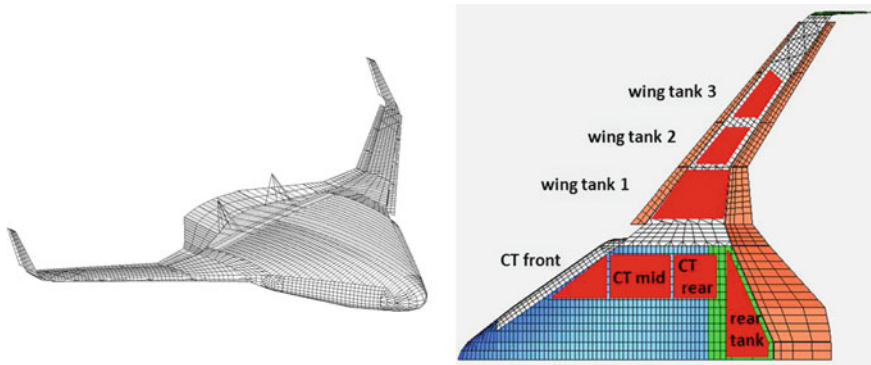


Fig. 3.55 FE model of the BWB aircraft structure (left) and fuel tank layout (right)

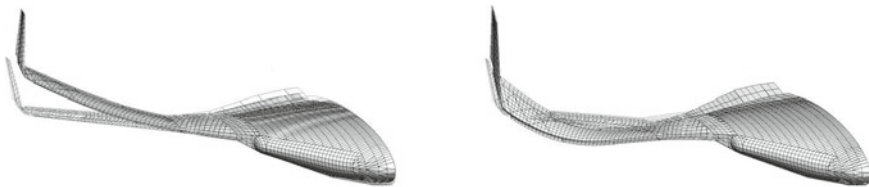


Fig. 3.56 First two symmetric elastic mode shapes

$$\left(-\omega^2 \mathbf{M}_{\text{struct}} + \mathbf{K}_{\text{struct}}\right) \mathbf{x}_{\text{struct}} = \mathbf{0} \quad (3.26)$$

The eigenvectors and natural frequencies are used as modal bases for each mass condition, comprised of 6 rigid-body (RB) modes Φ_r and a limited number of elastic modes Φ_e . The unit deflections of elastic modes are mass-normalized, leading to unitary modal mass matrices. To properly connect flight dynamic modes to RB modes, their deflections are normalized to 1m for translational modes, respectively 1rad for rotational modes (Fig. 3.56).

3.5.2 Aerodynamic Database

Steady aerodynamic analysis of the rigid aircraft, as well as unsteady aerodynamic analysis of the flexible aircraft has been performed with simplified, as well as high-order aerodynamic methods in subsonic and transonic regime. As usual in aeroelastic analysis, the unsteady aerodynamic database is computed for modal coordinates, that is, modal aerodynamic forces with respect to modal deflection. In order to account for the unsteady aerodynamics of control surfaces, additional control modes are introduced, which are defined by appropriate deflection of the aerodynamic degrees of freedom. Further, gust unsteady aerodynamic forces are included by a downwash distribution over the aircraft. The aeroelastic database is computed in frequency domain, assuming harmonic oscillation of mode shapes, control surface deflections, and gust downwash over a predefined frequency range. The reduced frequency k is applied here, which is a nondimensional quantity, usually applied in aeroelastic simulation, see (3.27).

$$k = \frac{\omega c}{2V_\infty} \quad (3.27)$$

Generalized aerodynamic forces (GAF), denoted by Q , are the unsteady aerodynamic forces on modal coordinates, normalized by dynamic pressure. The GAF Q_h are distinguished into forces due to modal perturbation Q_{hh} , control surface perturbation Q_{hc} , and gust excitation Q_{hg} . The modal forces in frequency domain can be

obtained by multiplication with modal deflections η , control surface deflections δ , and gust velocity w_g , see (3.28) as given in [9].

$$P_h(j\omega) = -q_\infty Q_{hh}(jk)\eta(j\omega) - q_\infty Q_{hc}(jk)\delta(j\omega) - q_\infty Q_{hg}(jk)\frac{w_g(j\omega)}{V_\infty} \quad (3.28)$$

3.5.3 Modification of GAF by Higher-Order Analysis Results

For the transonic regime, the GAF of some important structural modes are replaced with results from an unsteady CFD simulation, see Sect. 3.4. As the prescribed boundary motion in such unsteady aerodynamic computation has to be explicitly specified, one modal basis was selected.

By using a modal transformation rule, the GAF for the modal bases of all mass variants can be derived from the CFD-computed GAF of one modal basis. Let Q_{hh}^a be the GAF with respect to deflection of the mode shapes Φ_h^a and Q_{hc}^a with respect to control surface deflection. Then, the GAF Q_{hh}^b with respect to deflection of the mode shapes Φ_h^b , and Q_{hc}^b with respect to control surface deflection, are

$$\left[Q_{hh}^b(jk) \right] = \left[T_\phi^{ba} \right]^T \left[Q_{hh}^a(jk) \right] \left[T_\phi^{ba} \right] \quad (3.29)$$

$$\left[Q_{hc}^b(jk) \right] = \left[T_\phi^{ba} \right]^T \left[Q_{hc}^a(jk) \right] \quad (3.30)$$

with $\left[T_\phi^{ba} \right]$ as the least squares solution of the equation

$$\Phi_h^a T_\phi^{ba} = \Phi_h^b \quad (3.31)$$

By this transformation rule, the GAF of all modal bases in the transonic regime are replaced by CFD-computed results. The approximation error due to the linear transformation with a limited set of eigenvectors is comparably low.

3.5.4 Approximation of Aerodynamic Forces in the Laplace Domain

In order to derive equations of motion in the time domain, the GAF have to be expressed in Laplace domain first. This normally introduces a high number of additional degrees of freedom, to account for the time lags of aerodynamic forces. The minimum-state method, introduced by Karpel [5], is a rational function approximation method that accurately recovers the GAF in Laplace domain with only a

few additional degrees of freedom. The approximation rule of the GAF in Laplace domain, (3.32), is given in [9]:

$$Q_h(p) = \mathbf{A}_0 + \mathbf{A}_1 p + \mathbf{A}_2 p^2 - \mathbf{D}(\mathbf{I}p - \mathbf{R}^{-1})\mathbf{E}p, \tag{3.32}$$

where $p = s \frac{c}{2V_\infty}$ is the nondimensional Laplace variable. The approximation matrices \mathbf{A}_0 , \mathbf{A}_1 , \mathbf{A}_2 , \mathbf{D} , \mathbf{E} , and \mathbf{R} are applied to form the equations of motion of the time-domain aeroelastic simulation model.

3.5.5 Structural Outputs

Several structural displacement, velocity, and acceleration outputs are integrated into the model, to be applied for load alleviation in active control design. Therefore, the entries of the eigenvectors at specific degree of freedom positions are multiplied by modal deflections and their time derivatives. The nodal locations of the structural outputs are shown in Fig. 3.57. Further, force and moment outputs are applied at several positions over wingspan for left and right part of the aircraft. These are intended for a quantification of load alleviation techniques, applied in the control design studies.

3.5.6 Equations of Motion

The basis of the flight dynamics modal is the nonlinear 6 degrees of freedom Newton-Euler flight dynamic equations of motion. These are described by the angular and linear momentum conservation laws, (3.33) and (3.34), which can be found in several bibliographic references, such as [6]. The flight dynamic translational and rotational

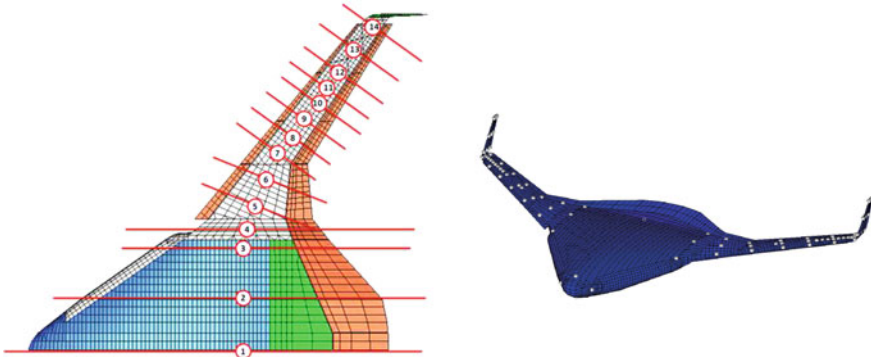


Fig. 3.57 Positions over wingspan for cut forces outputs (*left*), acceleration output positions over airframe (*right*)

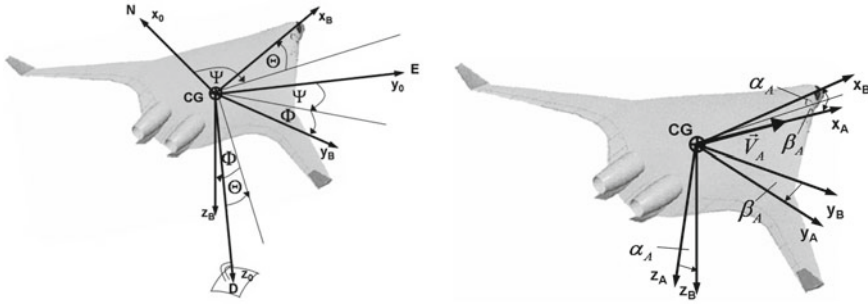


Fig. 3.58 Definition of NorthEastDown-System with inertial axes x_0, y_0, z_0 , body axes x_B, y_B, z_B , Euler angles Φ, Θ, Ψ , wind axes x_A, y_A, z_A , angle of attack α_A and side-slip angle β_A

degrees of freedom, V_b and Ω_b , are defined over body axes. Figure 3.58 provides an overview on inertial, aerodynamic and body axes, as well as attitude, incidence, and side slip.

$$m \{ \dot{V}_b + \Omega_b \times V_b - T_{be} g_e \} = F^{FD} + F_{AE}^{FD} + F_G^{FD} \quad (3.33)$$

$$J \dot{\Omega}_b + \Omega_b \times J \Omega_b = M^{FD} + M_{AE}^{FD} + M_G^{FD} \quad (3.34)$$

Here, m is the aircraft mass, J the inertial tensor, g_e gravitation acceleration in inertial axes and T_{be} the transformation matrix from inertial to body axes. The aerodynamic forces F^{FD} and moments M^{FD} from flight dynamic derivatives of the rigid aircraft are shown in (3.35) and (3.36).

$$F^{FD} = q_\infty S_{ref} T_{ba} \left(\begin{array}{c} \left[\begin{array}{c} C_D \\ C_Y \\ C_L \end{array} \right] + \left[\begin{array}{c} C_{Dp} \\ C_{Yp} \\ C_{Lp} \end{array} \right] p + \left[\begin{array}{c} C_{Dq} \\ C_{Yq} \\ C_{Lq} \end{array} \right] q + \left[\begin{array}{c} C_{Dr} \\ C_{Yr} \\ C_{Lr} \end{array} \right] r + \left[\begin{array}{c} C_{D\delta} \\ C_{Y\delta} \\ C_{L\delta} \end{array} \right] \delta \end{array} \right) \quad (3.35)$$

$$M^{FD} = q_\infty S_{ref} \frac{c}{2} T_{ba} \left(\begin{array}{c} \left[\begin{array}{c} C_l \\ C_m \\ C_n \end{array} \right] + \left[\begin{array}{c} C_{lp} \\ C_{mp} \\ C_{np} \end{array} \right] p + \left[\begin{array}{c} C_{lq} \\ C_{mq} \\ C_{nq} \end{array} \right] q + \left[\begin{array}{c} C_{lr} \\ C_{mr} \\ C_{nr} \end{array} \right] r + \left[\begin{array}{c} C_{l\delta} \\ C_{m\delta} \\ C_{n\delta} \end{array} \right] \delta \end{array} \right) \\ + (ARP - COG) \times F^{FD} \quad (3.36)$$

Here T_{ba} is the transformation matrix from aerodynamic to body axes, S_{ref} the aircraft reference surface, ARP and COG the coordinates of the aerodynamic reference point and center of gravity, and $C_{D,Y,L,l,m,p}$, etc., the flight dynamic derivatives. Aeroelastic coupling forces F_{AE}^{FD} and moments M_{AE}^{FD} , due to elastic modal motion are expressed in (3.37) by the rational function approximation matrices, introduced in (3.32).

$$\begin{Bmatrix} F_{AE}^{FD} \\ M_{AE}^{FD} \end{Bmatrix} = -q_{\infty} T_{be} \left(A_{re0} \eta_e + \left(\frac{c}{2V_{\infty}} \right) A_{re1} \dot{\eta}_e + \left(\frac{c}{2V_{\infty}} \right)^2 A_{re2} \ddot{\eta}_e + D_r x_a \right) \quad (3.37)$$

Gust aerodynamic forces and moments are expressed analogously by (3.38).

$$\begin{Bmatrix} F_G^{FD} \\ M_G^{FD} \end{Bmatrix} = -q_{\infty} T_{be} \left(A_{rg0} \frac{w_g}{V_{\infty}} + \left(\frac{c}{2V_{\infty}} \right) A_{rg1} \frac{\dot{w}_g}{V_{\infty}} \right) \quad (3.38)$$

The aeroelastic equations of motion are comprised by the modal inertial and elastic forces on the left-hand side, as well as aerodynamic forces due to flight dynamic, elastic, control surface, and turbulence perturbation, on the right-hand side of (3.39). Structural damping is neglected in this formulation.

$$\begin{aligned} & \mathbf{M}_{struct} \ddot{\eta}_e + \mathbf{K}_{struct} \eta_e \\ &= A_{e0} \begin{Bmatrix} \eta_r \\ \eta_e \\ \delta_c \\ \frac{1}{V_{\infty}} w_g \end{Bmatrix} + \left(\frac{c}{2V_{\infty}} \right) A_{e1} \begin{Bmatrix} \dot{\eta}_r \\ \dot{\eta}_e \\ \dot{\delta}_c \\ \frac{1}{V_{\infty}} \dot{w}_g \end{Bmatrix} + \left(\frac{c}{2V_{\infty}} \right)^2 A_{e2} \begin{Bmatrix} \ddot{\eta}_r \\ \ddot{\eta}_e \\ \ddot{\delta}_c \\ 0 \end{Bmatrix} + D_e x_1 \end{aligned} \quad (3.39)$$

For the coupling of flight dynamic motion to RB modes, η_r has to be transformed from inertial axes to body axes. The transformation rules are given by (3.40).

$$\eta_r = \begin{Bmatrix} -X \\ Y \\ -Z \\ -\Phi \\ \Theta \\ -\Psi \end{Bmatrix}, \quad \dot{\eta}_r = \begin{Bmatrix} -u \\ v + V_{\infty} \Psi \\ -w + V_{\infty} \Theta \\ -p \\ q \\ -r \end{Bmatrix}, \quad \text{and} \quad \ddot{\eta}_r = \begin{Bmatrix} -\dot{u} \\ \dot{v} + V_{\infty} q \\ -\dot{w} + V_{\infty} r \\ -\dot{p} \\ \dot{q} \\ -\dot{r} \end{Bmatrix} \quad (3.40)$$

The aeroelastic equations of motion are augmented by a lag (3.41), which accounts for time delays of unsteady aerodynamic forces. The first-order differential equation is solved for the lag states, which are coupled to the aeroelastic equations of motion (3.39).

$$\dot{x}_1 = \left(\frac{2V_{\infty}}{c} \right) [R] x_1 + [E] \begin{Bmatrix} \dot{\eta}_r \\ \dot{\eta}_e \\ \dot{\delta}_c \\ \frac{1}{V_{\infty}} \dot{w}_g \end{Bmatrix} \quad (3.41)$$

3.5.7 State-Space Model

The state-space form of the equations of motion is constructed by linearization of the combined flight dynamic and aeroelastic model, (3.33)–(3.41), at specified trim points. The resulting state, input and output vectors are assembled as shown in (3.42)–(3.44).

$$x = [\eta_r, \dot{\eta}_r, \eta_e, \dot{\eta}_e, x_1]^T, \quad (3.42)$$

$$u = [\delta^{\text{right}}, \delta^{\text{left}}, \dot{\delta}^{\text{right}}, \dot{\delta}^{\text{left}}, \eta^{2d}, \eta^{\text{vertical}}, \eta^{\text{lateral}}, \dot{\eta}^{2d}, \dot{\eta}^{\text{vertical}}, \dot{\eta}^{\text{lateral}}, F_{\text{Thrust}}, F_{\text{wingtip}}]^T, \quad (3.43)$$

$$y = [u^F, u^{\text{struct}}, \dot{u}^{\text{struct}}, \ddot{u}^{\text{struct}}, F^{\text{struct}}]^T. \quad (3.44)$$

References

1. Eliasson P (2002) EDGE a Navier-Stokes solver for unstructured grids. In: Proceedings of finite volumes for complex applications III, pp 527–534
2. European Commission (2014) Flying high with innovative aircraft concepts. http://ec.europa.eu/research/research-for-europe/transport-nacre_en.html
3. Fleischer D, Förster M, Breitsamter C (2011) Efficient CFD-based unsteady aerodynamics analysis. In: Proceedings of IFASD2011, international forum of aeroelasticity and structural dynamics, Stockholm
4. istworld (2014) Very efficient large aircraft. <http://www.ist-world.org/ProjectDetails.aspx?ProjectId=bc5fe779da034fe4926c266e1c644b66&SourceDatabaseId=9cd97ac2e51045e39c2ad6b86dce1ac2>
5. Karpel M (1981) Design for active and passive flutter suppression and gust alleviation, vol 3482. National Aeronautics and Space Administration, Scientific and Technical Information Branch
6. Lewis BL, Stevens FL (1992) Aircraft control and simulation. Wiley, New York
7. VSAERO—integral methods for potential and boundary layer flows (2014). <http://www.ami.aero/software-computing/amis-computational-fluid-dynamics-tools/vsaero/> Accessed 19 May 2014
8. Wildschek A, Stroscher F, Klimmek T, Šika Z, Vampola T, Valášek M, Gangsaas D, Aversa N, Berard A (2010) Gust load alleviation on a large blended wing body airliner. In: 27th International congress of the aeronautical sciences (ICAS)
9. ZONA Technology (2010) ZAERO theoretical manual. http://www.zonatech.com/Documentation/ZAERO_THEORETICAL_MANUAL_8.5.pdf. Current version 8.5 (2011). Accessed 8 July 2014